



# Spinit<sup>®</sup> - Magnetic Nanoparticle Improved Assay in a Centrifugal Microfluidics Platform

**Bavieche Jamnadas Samgi**

Thesis to obtain the Master of Science Degree in

**Engineering Physics**

Supervisors: Doctor João Manuel de Oliveira Garcia da Fonseca  
Professor Pedro Miguel Félix Brogueira

## **Examination Committee**

Chairperson: Professor Ana Maria Vergueiro Monteiro Cidade Mourão  
Supervisor: Doctor João Manuel de Oliveira Garcia da Fonseca  
Members of the Committee: Professor João Luís Maia Figueirinhas  
Doctor Abid Hussain

**October 2014**



## Acknowledgments

It is with immense gratitude that I acknowledge the support and help of my supervisor João Garcia da Fonseca.

I consider it a honour to work with Sandro Bordeira, whose knowledge and contagious cheerful spirit always allowed to move forward and keep the positivism during the bottleneck situations.

I would like to thank to my co-supervisor Pedro Brogueira for providing the setup to perform the AFM analysis and for the help during the analysis.

I would like to thank to all the Biosurfit team for the great working environment that I will most certainly miss. This thesis would not have been possible without the help from André Magalhães, Andreia Santos, Catarina Pereira, David Santos, Jorge Almeida, José Corte-Real, Lara Borges, Luís Martins, Luís Miguel, Nuno Reis, Pedro Esteves, Sandra Silva, and Vânia Silva.

I would like to thank to all my friends that were with me during this five years and made this journey even more memorable.

I would like to thank to Ana Paula and Ana Marta for all the insightful considerations that made this thesis more clear to everyone.

I cannot finish without thanking to Ana Marta for being there even when I was really hard to deal with and for always supporting me.

Last but not the least, I would like to thank to all my family - Kamlesha, Jamnadas, Darmeche -for helping me when I most needed.



## Resumo

Numa era marcada pelo envelhecimento da população verifica-se inevitavelmente um aumento da prevalência das doenças próprias desta faixa etária. A necessidade da aplicação imediata de terapêutica veio realçar a necessidade de estabelecer diagnósticos de forma célere. O desenvolvimento de ferramentas de diagnóstico primário imediato que possam ser aplicados no primeiro contacto com o doente reveste-se de uma grande importância.

A Biosurfit desenvolveu um dispositivo que permite obter resultados de análises sanguíneas em menos de 15 minutos. Para que este dispositivo possa ser útil a diversos centros de cuidados médicos, nomeadamente no que concerne à doença cardíaca isquémica, há certas características que se constituem como fundamentais, tais como a detecção de proteínas associadas a eventos isquémicos e cuja concentração sanguínea é inicialmente muito baixa.

A presente tese foca-se precisamente nesta questão: diminuir o limite de detecção do Spinit<sup>®</sup>, ou seja, incrementar a sua sensibilidade para a detecção de material biológico. Foi projectado um novo sistema de detecção que incorpora a manipulação de nanopartículas magnéticas com recurso a ímanes. Foi desenvolvido um ensaio modelo utilizando albumina de soro bovina biotinizada e nanopartículas com estreptavidina.

O projecto desenvolvido permitiu a amplificação do sinal em 50% para concentrações altas de analito, com um aumento do limite de detecção de albumina de soro bovino biotinizada de  $1 \mu\text{g ml}^{-1}$  para  $0.1 \mu\text{g ml}^{-1}$ , o que corresponde a um aumento de 10 vezes na capacidade de detecção. Assim, fica demonstrada a viabilidade da aplicação de nanopartículas magnéticas, com o protótipo construído, para detecção de proteínas no Spinit<sup>®</sup>.

**Palavras-chave:** Nanopartículas Magnéticas, Ressonância dos Plasmões de Superfície, Spinit<sup>®</sup>, Imunoensaio, Plataforma Microfluídica, Biotina-Estreptavidina



## Abstract

Population is ageing and associated with it there is an inevitable increase of the diseases associated with these ages. The need for a rapid diagnosis urges, so it is important to develop a diagnostic system that allows to have the results within the duration of a medical appointment.

Biosurfit developed an user-friendly instrument that gives results within 15 minutes. To achieve this goal it is important to be able to detect proteins that are present in a very low concentration such as some cardiac markers.

This thesis aims for decreasing the detection limit of Spinit<sup>®</sup>, that is to detect lower concentrations of proteins or other biological element. A new system using magnetic nanoparticles and their manipulation will be developed. This system will use magnets to attract the magnetic nanoparticles which will lead to a higher interaction efficiency. A model assay is developed to test the magnetic effect using biotinylated bovine serum albumin and streptavidin coated nanoparticles.

The results show that an increase of 50% is achieved for higher concentrations and the detection limit is pushed from  $1 \mu\text{g ml}^{-1}$  (using the standard system) to  $0.1 \mu\text{g ml}^{-1}$  when using the magnet. This thesis allows to demonstrate the feasibility of the application of magnetic nanoparticles, with the new prototype, to detect biological elements in Spinit<sup>®</sup>.

**Keywords:** Magnetic Nanoparticles, Surface Plasmon Resonance, Spinit<sup>®</sup>, Immunoassay, Microfluidic Platform, Biotin-Streptavidin



# Contents

---

	<b>Page</b>
Acknowledgments . . . . .	iii
Resumo . . . . .	v
Abstract . . . . .	vii
List of Tables . . . . .	xi
List of Figures . . . . .	xiv
List of Abbreviations . . . . .	xvi
<b>1 Introduction</b>	<b>1</b>
1.1 Biosensors . . . . .	1
1.1.1 Point of Care - POC . . . . .	5
1.2 SPR and Clinical Diagnostics . . . . .	6
1.3 Signal Amplification Strategies . . . . .	7
1.4 Thesis Outline . . . . .	11
1.5 Research Question . . . . .	11
<b>2 Grating Development</b>	<b>13</b>
2.1 Surface Plasmon Resonance - SPR . . . . .	13
2.1.1 Surface Plasmon Polaritons at Metal/Dielectric Interfaces . . . . .	14
2.1.2 Propagation Length and Penetration Depth . . . . .	17
2.1.3 Surface Plasmons Excitation Configurations . . . . .	18
2.1.4 Why do we need a new diffraction grating? . . . . .	20
2.2 PCGrate . . . . .	21
2.3 Results . . . . .	22
2.4 Produced Grating . . . . .	25
<b>3 Spinit<sup>®</sup> Assays</b>	<b>29</b>
3.1 Immunoassays & SPR . . . . .	29
3.2 Magnetic Nanoparticles and Magnetic Forces . . . . .	32
3.3 Material . . . . .	33
3.3.1 Spinit <sup>®</sup> . . . . .	33
3.3.2 Working Solutions . . . . .	35

3.3.3 Magnet & Magnet Holder Prototype . . . . .	36
3.4 Results . . . . .	39
3.4.1 Assay Development . . . . .	39
3.4.2 Dynamics Analysis . . . . .	45
3.4.3 Amplification Analysis . . . . .	47
<b>4 Conclusions</b>	<b>55</b>
4.1 Future Work . . . . .	57
<b>Bibliography</b>	<b>62</b>

# List of Tables

---

2.1 Grating simulation specifications for sine trapezoidal grating profile. . . . .	24
---	----



# List of Figures

---

1.1	Life expectancy at birth. . . . .	1
1.2	Biosensors market value evolution from 1996 to 2018. . . . .	2
1.3	“Biosensors and Bioelectronics” publication with “Biosensor” in the title from 1980 to 2014. . . . .	3
1.4	Overall structure of a biosensor. Figure from [5]. . . . .	3
1.5	Scheme of a cantilever biosensor. Figure from [1]. . . . .	4
1.6	Scheme of a conductometric biosensor. Figure from [1]. . . . .	4
1.7	Scheme of a fluorescent biosensor. Figure from [1]. . . . .	4
1.8	Clinical Tests Time Consumption. . . . .	6
1.9	Nanomaterials enhanced Surface Plasmon Resonance. Figure from [38]. . . . .	8
1.10	SPR sensing formulation proposed by[38]. Figure from [38]. . . . .	9
2.1	1 Dimension geometry. . . . .	15
2.2	Dielectric/Metal Geometry. . . . .	16
2.3	Dispersion relations for the different apparatus. Figure from [22]. . . . .	19
2.4	Prism configuration: Kretschmann (left) and Otto (right). . . . .	19
2.5	Reflectivity variation according to the gold layer thickness. Figure from [22]. . . . .	20
2.6	Grating coupling scheme. Figure from [12]. . . . .	20
2.7	Sine trapezoidal grating profile from PCGrate 6.1. . . . .	21
2.8	OS for the different gratings. . . . .	23
2.9	OSC for the different gratings. . . . .	23
2.10	OS for the different gratings not considering signal quality effects. . . . .	24
2.11	OSC for the different gratings. . . . .	25
2.12	Depth profile through AFM analysis. . . . .	26
2.13	Front view of the grating. . . . .	26
2.14	Isometric view of the grating. . . . .	26
3.1	Direct Assay. Figure from [9]. . . . .	29
3.2	Competitive Assay. Figure from [9]. . . . .	30
3.3	Inhibition Assay. Figure from [9]. . . . .	30
3.4	Sandwich Assay. Figure from [9]. . . . .	30
3.5	Example of a sensogram. . . . .	31

3.6	Magnetic moments behaviour with the external applied field. Figure from [21]. . . . .	32
3.7	SPR module and cartridge. Figure from [2]. . . . .	34
3.8	Dry-film cut profile. . . . .	35
3.9	Magnet holder with three pieces connected. . . . .	37
3.10	Magnet holder built with a 3D printer. . . . .	37
3.11	A sensogram resulting from a sandwich immunoassay using streptavidin+thiol on the surface, bsa-bt as analyte and 120 nm magnetic nanoparticles as amplification tags. . . . .	38
3.12	Test for the interaction between a pre-coated gold surface and 100 nm diameter streptavidin coated mnps from Ademtech. . . . .	40
3.13	Diagram of the intended assay. . . . .	41
3.14	Nsb for Spinit <sup>®</sup> 221 (with magnet) and Spinit <sup>®</sup> 223 (without magnet). Each assay was repeated twice. . . . .	42
3.15	Zone 0 comparison for both Spinit <sup>®</sup> . . . . .	43
3.16	Shift per zone for a disc rotating at 1600 rpm in both Spinit <sup>®</sup> . . . . .	44
3.17	Study of speed effect in Spinit <sup>®</sup> 221. . . . .	44
3.18	$D_{Max}$ for bsa-bt at 500 $\mu\text{g ml}^{-1}$ for Spinit <sup>®</sup> 221 (with magnet) and Spinit <sup>®</sup> 223 (without magnet). . . . .	46
3.19	$D_{Max}$ for bsa-bt at 100 $\mu\text{g ml}^{-1}$ for Spinit <sup>®</sup> 221 (with magnet) and Spinit <sup>®</sup> 223 (without magnet). . . . .	46
3.20	$D_{Max}$ for bsa-bt at 10 $\mu\text{g ml}^{-1}$ for Spinit <sup>®</sup> 221 (with magnet) and Spinit <sup>®</sup> 223 (without magnet). . . . .	46
3.21	$D_{Max}$ for bsa-bt at 5 $\mu\text{g ml}^{-1}$ Spinit <sup>®</sup> 221 (with magnet) and Spinit <sup>®</sup> 223 (without magnet). . . . .	46
3.22	$D_{Max}$ variation rate over the 11 detection zones. Spinit <sup>®</sup> 221 (with magnet) and Spinit <sup>®</sup> 223 (without magnet). . . . .	47
3.23	Association amplification increase with the magnet's introduction. . . . .	48
3.24	Shift per zone for different concentrations of bsa-bt in the Spinit <sup>®</sup> with a magnet. . . . .	49
3.25	Shift per zone for different concentrations of bsa-bt in the Spinit <sup>®</sup> without a magnet. . . . .	49
3.26	Shift in the last and first zone for different concentrations of bsa-bt in the Spinit <sup>®</sup> with a magnet (S221). . . . .	50
3.27	Shift in the last and first zone for different concentrations of bsa-bt in the Spinit <sup>®</sup> without a magnet (S223). . . . .	50
3.28	Relative shift from zone 1 to 10 compared to the first zone for the Spinit <sup>®</sup> with the magnet setup. . . . .	51
3.29	Relative shift from zone 1 to 10 compared to the first zone for the Spinit <sup>®</sup> without the magnet setup. . . . .	52
3.30	Logistic fit to zone 0 for both setups: with and without a magnet. . . . .	53
3.31	Zoom into the detection limit zone. . . . .	53
3.32	Amplification calculation using the fitted results. . . . .	54

# List of Abbreviations

---

<b>AFM</b>	Atomic Force Microscopy
<b>BRL</b>	Biological Recognition Layer
<b>CNC</b>	Computer Numerical Control
<b>CRP</b>	C-Reactive Protein
<b>LOD</b>	Limit of Detection
<b>LOQ</b>	Limit of Quantization
<b>MNP</b>	Magnetic Nanoparticle
<b>NP</b>	Nanoparticle
<b>NSB</b>	Non Specific Binding
<b>OS</b>	Overall Sensitivity
<b>OSC</b>	Overall Sensitivity Corrected
<b>PBS</b>	Phosphate Buffer Saline
<b>POC</b>	Point of Care
<b>POCT</b>	Point of Care Testing
<b>RPM</b>	Revolutions per Minute
<b>S221</b>	<i>Spinit</i> <sup>®</sup> 221
<b>S223</b>	<i>Spinit</i> <sup>®</sup> 223
<b>SMA</b>	Simple Moving Average
<b>SPP</b>	Surface Plasmons Polaritons
<b>SPR</b>	Surface Plasmon Resonance
<b>TAT</b>	Turn Around Time
<b>TE</b>	Transverse Electric

**TM** Transverse Magnetic

$k_a$  Association Constant

$k_d$  Dissociation Constant

**BSA-Bt** Biotinylated Bovine Serum Albumin

**FWHM** Full Width Half Maximum

# Introduction

---

The population on Earth is increasing and, due to the improved living and health conditions, the population is ageing. The population over 60 years of age has doubled since 1980 and in the coming years this difference will increase even further. Furthermore, the projections show that by 2030 the number of deaths due to cardiovascular diseases will be around 25 million, cancer will cause 13 million victims, and respiratory diseases will lead to 6.6 million deaths ([32]) heightening the demand for improved primary and secondary prevention. In the near future, governments will need to optimise the healthcare system to overcome this public health issue therefore investment on this area will grow immensely. A strategy for tackling this problem is to improve earlier diagnosis through new devices that make the entire diagnosis process more time and cost efficient.

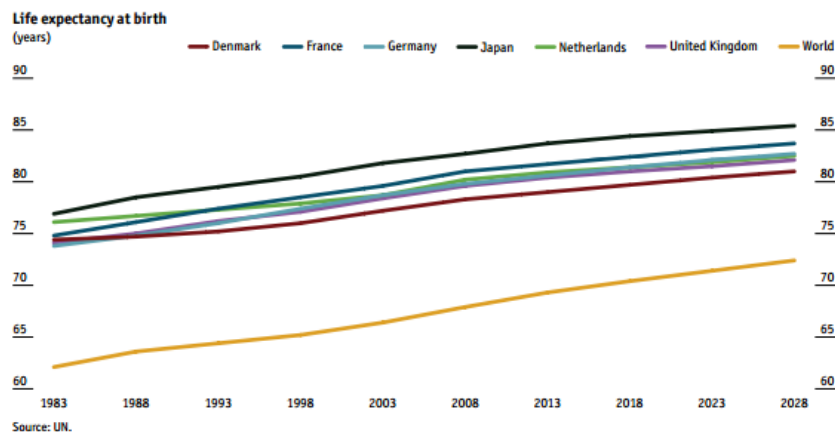


**Figure 1.1:** Life expectancy at birth from 1983 to 2028. Figure from U.N..

In addition to demographic drivers, costs also arise from technology, chronic conditions, obesity, and end of life care. There are a lot of drivers and one effective way of address all these drivers is using an early diagnosis which might help avoid both the suffering and costs associated with the progress of the disease. Hence, to keep and improve public health, developing structures which are able to detect several biological elements in a short amount of time in an affordable manner is imperative.

## 1.1 Biosensors

Biological recognition aiming to create better medical devices has been a hot topic for a while. For several decades there have been efforts to create devices capable of measuring biological elements such as proteins, enzymes, nucleic acids, or even cells. It all started in 1962 when Clark and Lyons built a

machine which was able to obtain quantitative data concerning glucose blood levels ([7]). Since then, this technology evolved. It became more sophisticated and its range of application increased from medical diagnostics to food safety, process control, environmental monitoring, military, and security applications.

Along with their growing development, **Biosensors** were given several definitions. Today, the one considered to be the more accurate was stated by the International Union of Pure and Applied Chemistry:

**"a self-contained integrated device which is capable of providing specific quantitative or semi-quantitative analytical information using a biological recognition element (biochemical receptor)"**

The impact of biosensors technology can be measured by assessing the market value associated with it, which amounts to millions of dollars. Figure 1.2 demonstrates a market that in the last ten years experienced a growth of 550% and keeps on growing. In 2014 the market is estimated to be around 13 billion US dollars (circa 10 thousand million euros) ([32]). To evaluate the growth in the biosensors

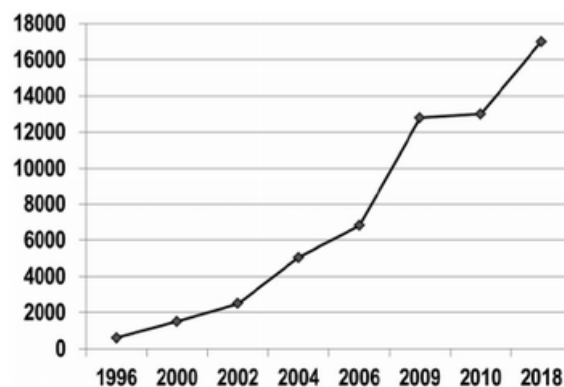


**Figure 1.2:** Biosensors market value evolution from 1996 to 2018. Horizontal axis represents the year and the vertical axis the biosensors market in millions of US dollars. Figure from [32].

technology, more than the business should be considered. The evolution in terms of academic publications should also be taken into account (Fig. 1.3). Considering "Biosensors and Bioelectronics" journal there is an obvious increase in the number of publications over the years, for example comparing 2000 and 2010 we can see a growth of 350% ([32]).

A biosensor can be divided into two components:

- recognition layer - sensitive structure which selects the binding analytes<sup>1</sup>,
- transducer - converts the interaction between the recognition element and the analyte into a physical signal, such as an electric signal

The function of the recognition layer is to allow the binding of specific biological elements, namely proteins. This selectivity can be achieved either by using the same principles inherent to the reactions within our body - biomolecular recognition such as antigen-antibody and protein-virus/bacteria affinity binding ([4]) or by using a chemical reaction on the sensor's surface that is functionalized with self-assembled monolayers or polymers coatings - catalytic binding ([4]). These layers have to be treated to

<sup>1</sup>element that is intended to be quantified/target component ([9])

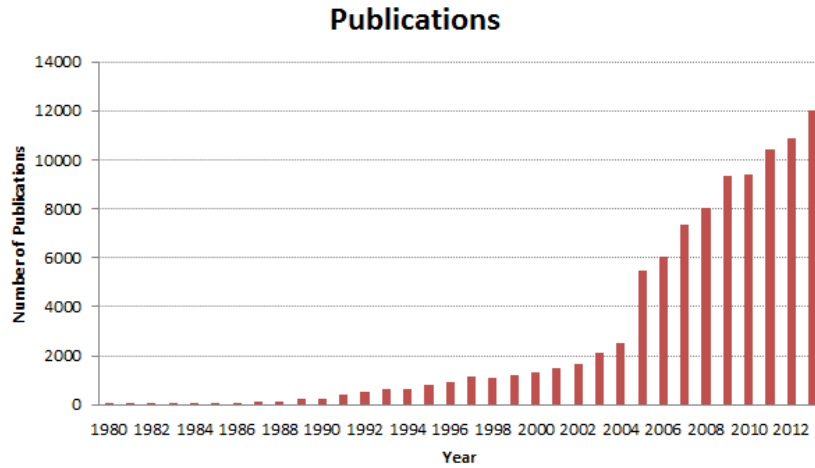


**Figure 1.3:** “Biosensors and Bioelectronics” publication with “Biosensor” in the title from 1980 to 2013.

achieve the immobilization of the biosensing elements so the recognition process can take place. The main techniques for immobilization are adsorption, entrapment, microencapsulation, cross-linking and covalent bonding ([31]).

This immobilization is one of the challenges that biosensors technology faces: with lowering concentrations of a certain analyte, high efficient markers are needed to allow the analyte detection without losses or functionality changes. On the other hand, if a sensor is not specific enough can corrupt the measurements, which result in false positives, lack of reproducibility and ultimately impair medical diagnosis. Hence, immobilization strategies are of a great importance to achieve the right specificity ([28]). Despite the importance of immobilization techniques, biosensors technology is classified according to the transduction principles associated with it. A biosensor is a device that intends to measure a biological component using a transducer to quantify the physical signal produced by the presence of the target biomolecule, as shown in figure 1.4.

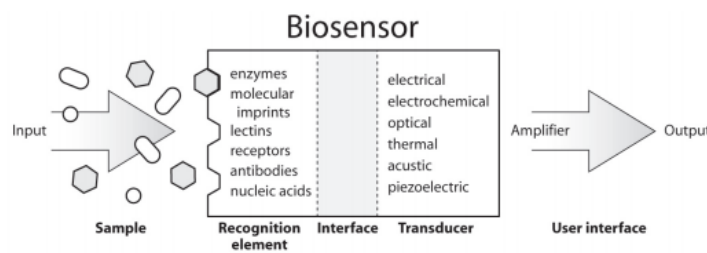


**Figure 1.4:** Overall structure of a biosensor. Figure from [5].

There are several kinds of physical signals, such as mechanical, electrical, optical, and magnetic. Besides this classification we can divide the biosensors technology into two different categories: label free and not label free. Label free means that there is no need of using any external probe to be able to create the conditions for detecting the target analyte. On the other hand, a biosensor which is not label free, does require a probe which connected with the analyte is able to create a signal proportional to the amount analyte.

In terms of mechanical transducers, we can use cantilevers (Fig. 1.5) which are structures that can

be used by measuring the deflection of its free end (Surface Stress Detection) or by calculating the resonance frequency due to mass change in the cantilever surface (Mass Detection). Both these detection mechanisms are label free.

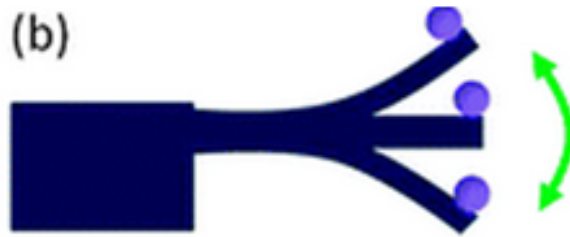


**Figure 1.5:** Scheme of a cantilever biosensor. Figure from [1].

Electrical transducers comprise three basic setups. The amperometric transducers use the electric current as detection mechanism. Another way of using electric transducers is by measuring the change in potential at the electrodes because of ions or chemical reactions near the electrodes - Potentiometric. Finally, the conductometric biosensors (Fig. 1.6) that take into account the conductance changes due to modifications of the ionic medium between the electrodes.

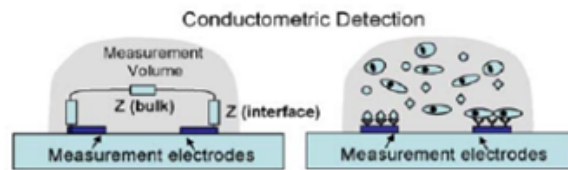


**Figure 1.6:** Scheme of a conductometric biosensor. Figure from [1].

Optical signals can also be used to detect biological elements. This optical detection technique is based on fluorescence which makes use of fluorescent markers which emit a specific wavelength that is enhanced or reduced due to the presence of the matching biomolecules. Other way of using optical probes

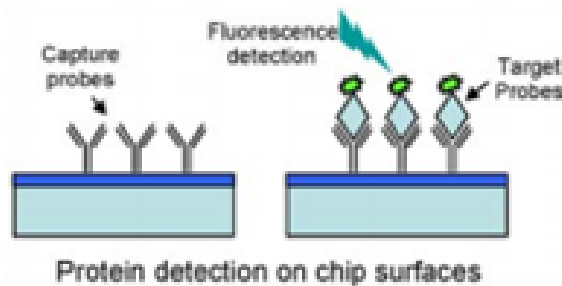


**Figure 1.7:** Scheme of a fluorescent biosensor. Figure from [1].

is through chemiluminescence which matches the energy release occurring due to chemical reactions. Both these approaches are not label free biosensors. An example of an optical label free transducer is the one based on surface plasmon resonance that uses the principle of total internal reflection due to excitation of surface plasmons to measure the presence of the analytes. This principle will be explained in more detail in section 2.1.

Finally, there is the group of transducers which use magnetic detection principles. Using magnetic labels we are able to take advantage of the low interaction of biomolecules with the magnetic field, and aim to a single particle sensitivity with the possibilities of magnetic manipulation. Giant magnetoresistance and Hall sensors are examples of this approach for analytes detection.

### 1.1.1 Point of Care - POC

Point of care testing (POCT) is a way of decentralizing the analysis required by the doctor. This system has to fulfil several conditions to be able to compete against the regular laboratory tests.

The requirements for a POC system are divided into two categories. The practicability related ones which take into account issues like the required skills and the sample type. And the reliability related ones, which deal with precision, detection limits, linearity, and the dynamic range. Neither of the two can be neglected, because if on one hand, the POC test has to yield robust and consistent results, on the other hand it has to be easy to operate so it can actually help to increase the doctor-patient interaction. The requirements for a POC system ([33]) are:

- Direct measurement in fluid,
- Full automation from sample to result,
- Small sample volume,
- Results within the duration of a usual appointment,
- Precision, sensitivity and accuracy,
- Internal calibration,
- Easy handling: minimal training and user friendly interface,
- Reduced need for maintenance,
- Simultaneous analyses of multiple analytes, and
- Low cost disposables.

POCT is commonly associated with the time length required for the test, however it goes beyond being just a rapid test. It can help to optimize the hospitalization and the patient-doctor appointments. Currently, if a patient goes to the doctor and has to do a laboratory assay the procedure is: Test Request → Go to the laboratory → Test → Gather test results → New Appointment. With a POCT, the results can be obtained and analysed at the moment of the appointment, therefore reducing immensely the time wasted by both patient and doctor.

Through this shortening of the testing process, POC technology can make the sampling less painful, reduce turn-around-time (TAT), avoid unnecessary hospital admissions, achieve earlier diagnosis, and earlier therapeutic interventions. However, there are also disadvantages such as the need for further confirmation of results, limited test menus, increased cost per test result, overuse due to availability, errors

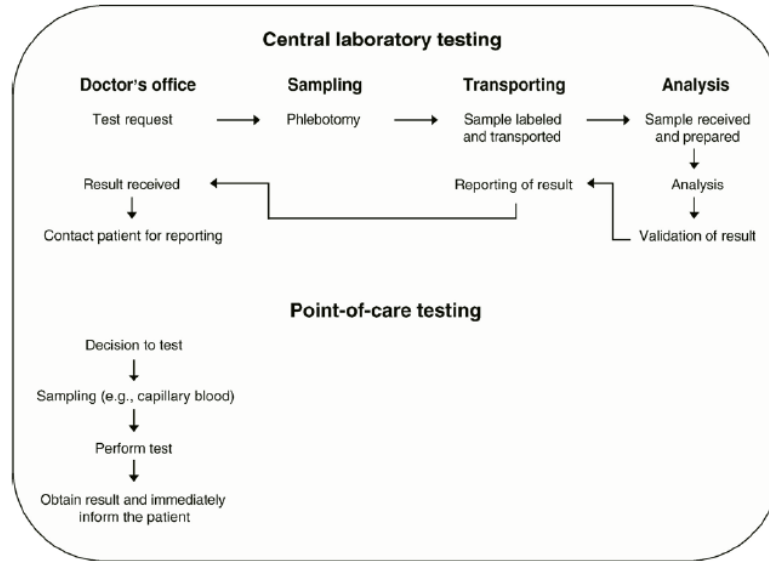


**Figure 1.8:** Comparison of the different types of clinical tests in terms of time consumption. Figure from [33].

due to untrained operators, and sample preparation variability. The POC immunotest is already used for several analytes: allergy markers, bacterias, cardiac markers, diabetes markers, or tumour markers; mainly as detection or diagnosis mechanism.

POCT analysers can be divided into several groups ([18]) :

- Qualitative strip based- A test that discriminate plus and minus. The signal is obtained through simple visualization or by optical detection. The detection mechanism varies from chemical-indicator reactions to immunological reactions. It is commonly used in pregnancy tests, detection of blood in stool, or urine dipstick analyses.
- Unit Use - Quantitative device in which the reaction take place in a test strip. The reader is only used to read the result from the strip that is used only once. Examples of available systems are: EPOC Smart Card, 4cast-Chip & Reader, In2It HbA1c analyser, and Afinion AS100 Analyzer.
- Bench Top - These devices are more complex and are thought to be used in the doctor's room. These devices are based on several analytical principles: spectrophotometric (Piccolo, Triage Meter Pro, Reflotron, MICT Benchtop System) , haematological particle counting (PocH-100i), immunoassay (Pathfast, Radiometer AQT90), and sensor-based blood-gas analysis.

## 1.2 SPR and Clinical Diagnostics

Surface plasmon resonance application for clinical tests has been attracting more interest in recent years ([9]). Several studies involving biological variables such as C-Reactive protein, human ferritin and prostate-specific antigen demonstrated the capacity of detecting these clinically relevant analytes. There are devices from different companies such as Biacore, IBIS, GWC Technologies, Biosensing Instruments, K-Mac, and Lumera available in the market. However, these equipments aim for the research market and

not for clinical diagnosis.

Detection through SPR is considered one of the most adequate to fulfil POC requirements, for several reasons ([9]):

- It allows for **rapid** detection since it is based on the refractive index changes due to the binding event which are translated into a value as they occur.
- It is capable of **direct detection** of many important analytes. When the sensitivity is not enough to detect the analyte, **adaptability** towards amplification is feasible.
- Optics is a major concern for the SPR imaging. Since this can be **miniaturized**, it can fit in a POC system.
- It allows for **simultaneous detection of multiple events** using spatially addressed capture arrays.
- Along with the development in microfluidics, preconditioning of **small sample volumes** is possible.

These devices, are commercially available, as Spinit<sup>®</sup> is. All of them are aiming for the reduction of the limit of quantization (LOQ). Therefore, several amplification strategies are applied to increase the signal for the lower concentrations.

### 1.3 Signal Amplification Strategies

With the variety of sensors available, presently the focus relies on the detection of low molecular weight analytes (<400 Da) which are present in very low concentrations ([38]). SPR based sensors present several advantages such as a rapid, direct, and not label dependent detection. The miniaturization and adaptability for novel amplification techniques are also features to underline their importance ([9]). Despite all these advantages, the usual setup is not sensitive enough to detect analytes with small molecular weight such as cardiac troponins, cancer biomarkers, and hormones ([38]).

The ordinary SPR and the localized SPR are the two main type of surface plasmons. The first one corresponds to the surface plasmons resonance due to an excitation on thin metal films using a prism or grating with a propagation length of hundreds of micrometers ([38]). The second one refers to the excitation of surface plasmons only on the surface of nanostructures which can be tuned by size, shape, and composition ([38]).

The challenge for the SPR sensors is to detect small molecular weight (< 8kDa) and low concentrations (<1 pM). To operate in this regime, several sensitivity-enhancement approaches have been applied. Figure 1.9 shows the different methods used to enhance sensitivity based on nanomaterials and a bird's-eye view of the current state-of-the-art strategies to improve the SPR signal.

There are several methods evolving nanomaterials to improve SPR sensing: the electric field increase due to the coupling of the LSPR on the nanomaterials surface and the ordinary surface plasmons resonance on the sensing film. There is also an increase of mass load to achieve greater perturbations on the film. In addition, the charge transfer from the nanomaterial to the surface film is used to enhance the evanescent

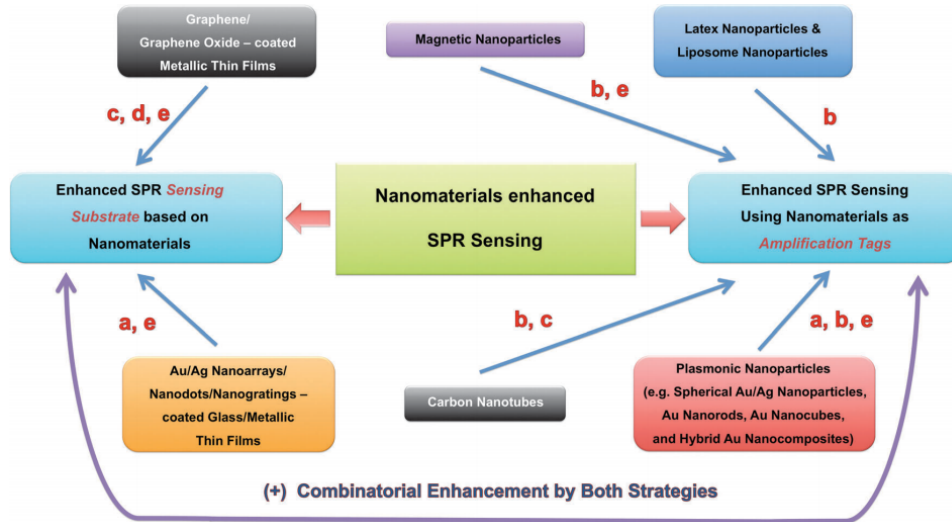


**Figure 1.9:** Nanomaterials enhanced Surface Plasmon Resonance. Figure from [38].

wave. The adsorption is also improved by using the pi-stacking force between the analyte and the nanomaterial surface. Finally, the catalytic activity of functionalized nanomaterials as a further trigger for secondary signal amplification is also an option to enhance the SPR signal.

Figure 1.9 depicts that there are two main groups of strategies:

- enhanced SPR **sensing substrate** based on nanomaterials,
- enhanced SPR sensing using nanomaterials as **amplification tags**.

One of the most commonly used techniques for amplifying SPR signal consists in employing gold nanoparticles as amplification tags. As the localized SPR peaks of these nanoparticles are dependent on their size, shape, and dielectric constants, the setup can be optimised by choosing the gold nanoparticle features that best couple the LSPR and the ordinary SPR. Shuwen Zeng et al. showed through a size-dependent signal response analysis which showed that 40 nm diameter Au nanoparticle at 5 nm from the sensing surface offer the best amplification factor: norm of electric field is 4.5 times higher with 40 nm nanoparticles than 80 nm nanoparticles [37]. Hence, this work can be used as a guide for tuning the gold nanoparticle enhanced SPR.

An important application of SPR sensing are the immunoassays based on protein biomarkers and antibodies, since they are used for both preclinical and clinical assessments. However, there are many proteins either with a low molecular weight or at low concentration which are not detectable by the conventional SPR sensor. To increase the dynamic range, Lyon et al. have developed a sandwich immunoassay with human immunoglobulin (h - IgG). They functionalized colloidal gold nanoparticles with secondary antibodies - goat monoclonal anti-human IgG Fc-specific. The results showed a 25-fold increase in SPR sensitivity with a detection limit of 6.7 pM for h-IgG ([19]).

As a method for further improvement of sensitivity, Caos et al. proposed a gold nanoparticles formulation for sensing anti-glutamic acid decarboxylase antibody (anti-GAD- Ab) used for the diagnosis of insulin-dependent diabetes mellitus. In their setup, Au NPs were treated to form an enzyme-immunogold complex (Au NPs - anti IgG-HRP). The first step of the assay consisted on binding the anti-GAD-Ab

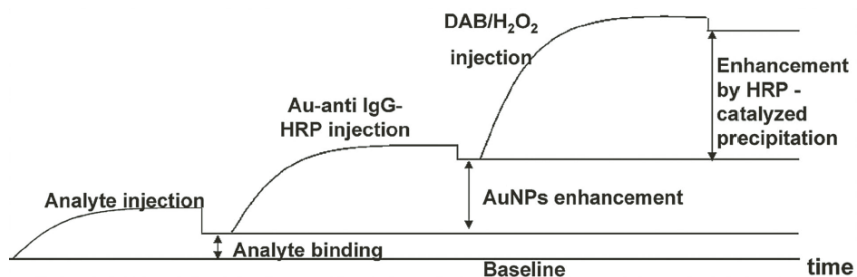


**Figure 1.10:** SPR sensing formulation proposed by [38]. Figure from [38].

to the GAD on the sensor surface which lead to a small signal change. Second, the AuNP - anti IgG - HRP complex was introduced as an amplification tag which was detected due to the reaction between the anti-IgG and the anti-GAD-Ab. Finally, the second amplification was achieved injecting a  $DAB - H_2O_2$  which reacted with the HRP leading to the deposition of an oxidized product on the sensor surface. This configuration allowed for a LOD of  $0.03 \text{ ng ml}^{-1}$  of anti-GAD-Ab ([38]).

Law et al. used gold nanorods conjugated to anti-rabbit IgG in a setup with a fixed wavelength of 785 nm as a light source and several aspect ratios were tested - 530, 642, 718, 772. The detection limit was estimated to be around  $40 \text{ pg ml}^{-1}$  for the NR642-anti-IgG versus  $0.9 \text{ ng ml}^{-1}$  without using the nanorods therefore a 23-fold increase in sensitivity was demonstrated ([16]).

Gold nanoarrays with diffractive coupling of localized plasmon resonances were designed by Kravets et al. showing a high phase sensitivity for single-molecule detection. The surface plasmon excitation is achieved using a geometry which allows for the attenuated total reflection through a visible light source. Both wavelength and resonance angle can be modified by manipulating the periodicity of the nanoarrays. This group used several nanoarrays structures such as nanodots, double dots, Au dumbbells, stripes and arrays of holes in PMMA-Au double layers. The double dot structure showed the best performance and it was capable of detecting a solution of streptavidine at 10 pM ([14]).

A SPR signal amplification strategy based on creating a binding matrix by electropolymerizing a bis-aniline-cross-linked Au NPs composite on the sensing surface was created to detect TNT molecules. In addition, Au NPs were functionalized with a mixed monolayer of thioaniline and mercaptoethane sulfonate to serve as amplification tags. NPs were first electropolymerized onto to the surface as imprinted sites that along with picric acid (similar to a TNT molecule) formed  $\pi$ -donor-acceptor complexes. The final version of the sensing film was obtained with the reaction between a 0.1 M solution and the picric acid molecules that left the  $\pi$ -donor sites to interact with the TNT molecules. The detection limit for this configuration was approximately 10 pM ([25]).

Additionally, structures such as magnetic nanoparticles, carbon based nanomaterials, silver nanoparticles, latex nanoparticles and liposome nanoparticles were created to detect analytes with small molecular weight or present in small quantities.

Magnetic nanoparticles (MNPs) have a high area-to-volume ratio so encompass high surface energy for chemical reactions. These nanoparticles also allow the conjugation of several biomolecules due to versatile surface modification chemistry, have a high molecular weight, a high refractive index, and are cost-effective to synthesize, therefore being an appealing case study for SPR signal enhancement.

Magnetic nanobeads were used by Teramura et al. to detect brain natriuretic peptide (BNP), an indicator of heart failure. In this experiment, the sensing film was functionalized with monolayers of carboxyl-group terminated with alkanethiol and the primary monoclonal antibodies, specific to the natriuretic peptide, were covalently immobilized onto the sensing surface. The first step of the assay was the injection of the BNP solution followed by the biotin-labeled secondary antibodies (sandwich immunoassay). Next, the amplification was carried on with several layers of alternated biotin-labeled anti-streptavidin antibody and 50 nm streptavidin-cojugated nanobeads. The LOD for BNP was of  $25 \text{ pg ml}^{-1}$  ([30]).

Magnetic nanoparticles ( $Fe_3O_4$ ) were used as an amplification tag to detect adenosine with a range from 10 nM to  $10^4$  nM. The nanoparticles were built by pyrolysis of iron carboxylate in an organic phase. The transition to the aqueous phase was achieved using a hydrophilic functional group. Two different sizes - 14.51 nm and 32.82 nm - were used in this study. These nanoparticles were then bounded to the thiol modified sensing film. Results showed that larger NPs and larger NPs concentration had a larger signal change which was explained by the molecular weight and the increase of the surface coverage. The study for the adenosine detection was based on an indirect competitive inhibition assay. The first step included the functionalization of nanoparticles with antiadenosine aptamers and the surface functionalization with the complementary antiadenosine aptamers. Next, the bioconjugated magnetic NPs solution was introduced into the system leading to a larger SPR signal change due to the interaction between the complementary antiadenosine aptamers and antiadenosine. Lastly, the addition of target adenosine to the magnetic NPs solution created nanoparticles with reduced binding capacity leading to a smaller SPR signal change ([34]).

MNPs combined with magnets were studied in 2011. The setup used a metallic diffraction grating sensor functionalized with recognition antibodies. On the other hand, the magnetic nanoparticles were coated with conjugated antibodies serving both as label due to the increase of the refractive index and as a faster way of recognizing due to the magnetic field manipulation. Tests on  $\beta hCG$  were performed and the results show an increase of approximately 4 orders of magnitude (compared to the direct detection mechanism) in sensitivity to 0.45 pM ([35]).

Graphene coated Au-Ag thin films were tested with a prism coupling system with angular variation. Results showed an increased contrast at the resonance angle compared to the structure without the thin film. Non specific interaction analysis showed that the association constant for bovine serum albumin (bsa) on the new configuration was three times smaller ( $2.4 \times 10^{-5} \text{ Ms}^{-1}$ ) than in anti-bsa modified capture Au sensing ( $7.4 \times 10^{-5} \text{ Ms}^{-1}$ ) ([27]).

Graphene oxide sheet-coated Au thin film was used to test human IgG. In this experiment the graphene oxide was assembled onto the sensing film by strong electrostatic forces that resulted on a monolayer or bilayer with high surface flatness. The SPR sensor consisted on a wavelength modulation that allowed for the antibody-antigen monitorization. First, the graphene oxide was functionalized anti-human IgG, then the target analyte was introduced in different concentrations. This study reported a four times more sensitive configuration than the conventional gold sensing film ([11]).

A different way of using carbon atoms is through carbon nanotubes (CNTs ). A study in 2011, shows

the possibility of using these structures to detect human erythropoietin (EPO) and human granulocyte macrophage colony-stimulating factor (GM-CSF) molecules. CNTs were functionalized with secondary antibodies that were specific to EPO and GM-CSF and surface with the capture antibodies for EPO and GM-CSF. Results showed an improvement of 30 times (with a detection limit of  $0.1 \text{ ng ml}^{-1}$ ) when CNTs were used compared to the amplification tag free immunoassay ([17]).

## 1.4 Thesis Outline

This thesis is divided into four main chapters: Introduction, Simulation, Spinit Assays, and Conclusions.

Chapter two is based on the simulations ran to produce a new diffraction grating disc. Therefore, it starts with the explanation of the physical principle used to detect biological elements - Surface Plasmon Resonance. Furthermore, the results from the simulations are presented and discussed. The last part concerns the atomic force microscopy analysis of the produced grating.

Chapter three introduces the basics of immunoassays and magnetism to set the ground for the experiments which will be described afterwards. The material and both initial and final setups are described. Along with the material, the methods for the assay analysis are explained. Finally, the main conclusions from the initial testing are presented followed by the analysis of the magnet implementation.

Chapter four is a sum up of all the work carried on during this thesis. The discussion of the results and the conclusions resulting from this project are presented. In addition, future work is proposed.

## 1.5 Research Question

Biosurfit created a device - Spinit<sup>®</sup>- which uses disc shaped disposable cartridges. The assay uses a drop of blood and yields results within 15 minutes. These discs contain a microfluidics system which allows the detection of the C-Reactive protein with a quantification limit of  $5 \mu\text{g ml}^{-1}$ . Even though this detection limit is enough for detecting the usual amounts of these proteins present in blood, there are several other proteins such as cardiac troponins which are liberated in low concentrations into the blood stream and are not detected with the current sensing capabilities. The improvement of the quantification and detection limits is a major focus on both academic and applied research. With this thesis, we aim for the application of a magnetic nanoparticle assay to decrease the LOD. This decrease on the LOD is intend to be achieved through the development of a new diffraction grating and the implementation of MNPs along with a magnet to increase the throughput of nanoparticles near the surface. The core of this thesis can be summarized with the following research question:

**How to incorporate a magnetic nanoparticle assay into Spinit<sup>®</sup>?**



# Grating Development

---

## 2.1 Surface Plasmon Resonance - SPR

Surface plasmons were first observed in 1902 by R. M. Wood ([36]) which he described as anomalous diffraction. He observed dark and bright bands of light using an optical grating and an incandescent lamp. At the time, he realized that this result was possible only for p-polarized light and named it “singular anomalies”. The first theoretical breakthrough on this matter was presented by U. Fano ([8]) in 1941 explaining surface plasmons excitation through surface waves. In the 1950’s the excitation of plasmons due electrons was presented by Pines and Bohm ([3]) and in 1957 R.H. Ritchie postulated the existence of surface plasmons in thin metal films penetrated by electrons ([26]). Despite the early discovery, the optical methods to the surface plasmon excitation were presented only in late 60’s: Kretchman ([15]) and Otto ([23]) used the attenuated total reflection to demonstrate the optical excitation of surface plasmons explaining, finally, the physical principle supporting SPR.

In the 1970’s, a SPR based sensing technique was used to characterize thin films. Further investigation into SPR applications allowed to build sensors to evaluate bio-molecular interactions. The 1980’s brought the first company founded based on a SPR based machine - Pharmacia Biosensor AB (now Biacore AB). During the years, development in SPR sensors led to a wide range of applications such as medical diagnosis (Cancer Biomarkers, Hormones, Pathogens, etc.), bioanalysis, biomolecular interactions, biopharmaceutics, surface enhanced spectroscopes which lead to the construction of several systems that are now available commercially.

This phenomena is a result from an interaction between a material and an external magnetic field. To describe such phenomena, the dielectric function is essential so it is important to describe it mathematically. In an insulator, such as proteins, the electrons are strongly localized at the atomic sites and only strong electric fields might give them some mobility. For these materials the real part of the dielectric function is small and positive while the imaginary part is approximately zero. Metals, on the other hand, possess electrons with mobility that are able to move to different sites when acted by an external electric field. At the macroscopic level, this peculiarity gives rise to the typical metallic luster, ductility, heat conduction and electric currents. The real part of the dielectric function is negative and small while the imaginary part is positive. The dielectric properties of metals can be described by the free electron gas model. There is a wide range of frequencies in which a metal can be described by a plasma model ([20]), for noble metals the limitation occurs at the visible frequencies while for alkali metals the range extends up to the ultraviolet. In this model, the lattice potential and electron - electron interactions are

not considered and the band structure aspects are incorporated into the effective optical mass  $m$ . When applying an electromagnetic field, the electrons oscillate and their motion is damped via collisions that occur at a characteristic frequency  $\gamma = 1/\tau$  where  $\tau$  represents the relaxation time of the free electron gas ( $\approx 10^{-14}$  s at room temperature). Considering this framework the dielectric function is given by:

$$\epsilon(\omega) = 1 - \frac{\omega_p^2}{\omega^2 + i\gamma\omega} , \quad (2.1)$$

where  $\omega$  is the applied field frequency and  $\omega_p$  is the plasma frequency of the free electron gas:

$$\omega_p^2 = \frac{ne^2}{\epsilon_0 m} , \quad (2.2)$$

where  $n_e$  is electron density,  $e$  the electron charge and  $m_e$  the effective electron mass. In addition to these bulk plasmons, there are surface plasmons.

### 2.1.1 Surface Plasmon Polaritons at Metal/Dielectric Interfaces

Surface plasmons can be seen as an oscillation of free electron density. The coupling of the electromagnetic wave to the oscillations of electrons on a metal surface leads to the creation of an electromagnetic surface wave. These electromagnetic waves are excitations that propagate at the interface between a dielectric and a conductor, evanescently confined in the perpendicular direction. Maxwell's equations can be used to obtain the dispersion relation of surface plasmons:

$$\left[ \nabla \times \vec{E} \right] = - \frac{d\vec{B}}{dt} , \quad (2.3)$$

and

$$\left[ \nabla \times \vec{H} \right] = \vec{J} + \frac{d\vec{D}}{dt} . \quad (2.4)$$

Combining these two equations and assuming that there are not external stimuli, the wave equation is:

$$\left[ \nabla \times \left[ \nabla \times \vec{E} \right] \right] = -\mu_0 \frac{\partial^2 \vec{D}}{\partial t^2} , \quad (2.5)$$

which considering the vectorial identity  $\left[ \nabla \times \left[ \nabla \times \vec{E} \right] \right] = \nabla(\nabla \cdot \vec{E}) - \nabla^2 \vec{E}$  and that  $\nabla \cdot \vec{E} = \frac{\rho}{\epsilon_0} = 0$

$$\nabla^2 \vec{E} - \frac{\epsilon}{c^2} \frac{\partial^2 \vec{E}}{\partial t^2} = 0 . \quad (2.6)$$

If the electric field is assumed to have a harmonic time dependence, described by  $\vec{E}(\vec{r}, t) = \vec{E}(\vec{r})e^{-i\omega t}$ .

This leads to the Helmholtz equation:

$$\nabla^2 \vec{E} - \left( \frac{\omega}{c} \right)^2 \epsilon \vec{E} = 0 . \quad (2.7)$$

Without loss of generality, the equation 2.7 can be applied to an one-dimensional problem represented in figure 2.1.

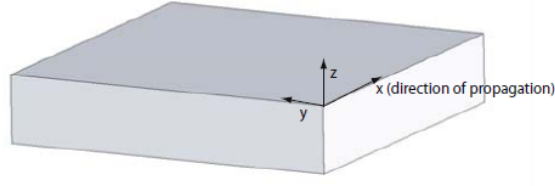


**Figure 2.1:** 1D geometry. Figure from [20].

In this problem, the waves propagate along the x-direction so the electric field can be described as  $\vec{E}(x, y, z) = E(z)e^{i\beta x}$ , where  $\beta$  represents the propagation constant of the wave and it is the result of the wave vector in the direction of propagation so the wave equation is:

$$\frac{\partial^2 \vec{E}(z)}{\partial z^2} + (k_0^2 \epsilon - \beta^2) \vec{E} = 0 . \quad (2.8)$$

Applying equations 2.3 and 2.4 and assuming a harmonic time dependence ( $\frac{\partial}{\partial t} = -i\omega$ ) we can obtain the system of equations:

$$\frac{\partial E_y}{\partial z} = -i\omega\mu_0 H_x , \quad (2.9a)$$

$$\frac{\partial E_x}{\partial z} - i\beta E_z = i\omega\mu_0 H_y , \quad (2.9b)$$

$$i\beta E_y = i\omega\mu_0 H_z , \quad (2.9c)$$

$$\frac{\partial H_y}{\partial z} = i\omega\epsilon_0 \epsilon E_x , \quad (2.9d)$$

$$\frac{\partial H_x}{\partial z} - i\beta H_z = -i\omega\epsilon_0 \epsilon E_y , \quad (2.9e)$$

$$i\beta H_y = -i\omega\epsilon_0 \epsilon E_z . \quad (2.9f)$$

The equations 2.9 allow for two sets of solutions: one for the transverse magnetic - TM or p-polarized - and one for the transverse electric - TE or s-polarized. The transverse magnetic is characterized by a magnetic field component along the y-axis while the transverse electric is characterized by an electric field along the y-axis. For the TM modes, the system is simplified to:

$$E_x = -i \frac{1}{\omega\epsilon_0 \epsilon} \frac{\partial H_y}{\partial z} , \quad (2.10a)$$

$$E_z = -\frac{\beta}{\omega\epsilon_0 \epsilon} H_y . \quad (2.10b)$$

On the other hand, TE mode yields:

$$H_x = i \frac{1}{\omega\mu_0} \frac{\partial E_y}{\partial z} , \quad (2.11a)$$

$$H_z = \frac{\beta}{\omega\mu_0} E_y . \quad (2.11b)$$

The simplest geometry able to sustain surface plasmons polaritons is a flat interface between a dielectric and conducting material. The dielectric space is characterized by a positive real dielectric constant ( $\epsilon_{dielectric}$ ) and the conducting space by a dielectric function with the real part being negative.



**Figure 2.2:** Dielectric-Metal geometry. Figure from [20].

The solutions that give rise to surface plasmons are confined to the interface, that is, solutions in which there is an evanescent decay in the perpendicular direction ( $z$  axis). First, we apply the continuity equations for the TE modes. Hence, using equations 2.11, we get the components for both magnetic and electric field for  $z > 0$ :

$$E_y = A_{dielectric} e^{i\beta x} e^{-k_{dielectric} z} , \quad (2.12a)$$

$$H_x = -i A_{dielectric} \frac{1}{\omega \mu_0} k_{dielectric} e^{i\beta x} e^{-k_{dielectric} z} , \quad (2.12b)$$

$$H_z = A_{dielectric} \frac{\beta}{\omega \mu_0} e^{i\beta x} e^{-k_{dielectric} z} , \quad (2.12c)$$

and for  $z < 0$ :

$$E_y = A_{metal} e^{i\beta x} e^{k_{metal} z} , \quad (2.13a)$$

$$H_x = i A_{metal} \frac{1}{\omega \mu_0} k_{metal} e^{i\beta x} e^{k_{metal} z} , \quad (2.13b)$$

$$H_z = A_{metal} \frac{\beta}{\omega \mu_0} e^{i\beta x} e^{k_{metal} z} . \quad (2.13c)$$

The continuity conditions at the interface for the  $\mathbf{E}$  field and the  $\mathbf{H}$  field are  $E_{y,dielectric} = E_{y,metal}$  and  $H_{x,dielectric} = H_{x,metal}$  that leads to

$$A_{dielectric} = A_{metal} , \quad (2.14a)$$

$$A_{metal} k_{metal} + A_{dielectric} k_{dielectric} = 0 , \quad (2.14b)$$

$$\Rightarrow A_{metal} (k_{metal} + k_{dielectric}) = 0 . \quad (2.14c)$$

To have a confined solution, both  $\Re[k_{metal}]$  and  $\Re[k_{dielectric}]$  must be positive therefore the condition is

true only when  $A_{metal} = A_{dielectric} = 0$ . In summary, it is not possible to have a surface mode in a TE polarization mode.

Applying the same analysis to the TM mode, for  $z > 0$ :

$$H_y = A_{dielectric} e^{i\beta x} e^{-k_{dielectric} z} , \quad (2.15a)$$

$$E_x = i A_{dielectric} \frac{1}{\omega \epsilon_0 \epsilon_{dielectric}} k_{dielectric} e^{i\beta x} e^{-k_{dielectric} z} , \quad (2.15b)$$

$$E_z = -A_{dielectric} \frac{\beta}{\omega \epsilon_0 \epsilon_{dielectric}} e^{i\beta x} e^{-k_{dielectric} z} , \quad (2.15c)$$

and for  $z < 0$ :

$$H_y = A_{metal} e^{i\beta x} e^{k_{metal} z} , \quad (2.16a)$$

$$E_x = -i A_{metal} \frac{1}{\omega \epsilon_0 \epsilon_{metal}} k_{metal} e^{i\beta x} e^{k_{metal} z} , \quad (2.16b)$$

$$E_z = -A_{metal} \frac{\beta}{\omega \epsilon_0 \epsilon_{metal}} e^{i\beta x} e^{k_{metal} z} . \quad (2.16c)$$

The continuity conditions at the interface for the  $\mathbf{E}$  field and the  $\mathbf{H}$  field are  $\epsilon_{dielectric} E_{z,dielectric} = \epsilon_{metal} E_{z,metal}$  and  $H_{y,dielectric} = H_{y,metal}$  that leads to

$$A_{dielectric} = A_{metal} , \quad (2.17a)$$

$$\frac{k_{dielectric}}{k_{metal}} = -\frac{\epsilon_{dielectric}}{\epsilon_{metal}} . \quad (2.17b)$$

For the confinement to be possible, there is the need for a  $\Re[\epsilon_{metal}] < 0$ , which means that  $\epsilon_{dielectric}$  must be positive, so the surface waves exist in case the interface is between two materials with opposite signs of the real part of the dielectric permittivities. Incorporating the result from 2.17 into the wave equation, it is possible to obtain the dispersion relation of SPPs:

$$\beta = \frac{\omega}{c} \sqrt{\frac{\epsilon_{metal} \epsilon_{dielectric}}{\epsilon_{metal} + \epsilon_{dielectric}}} . \quad (2.18)$$

Surface plasmon resonance exist only for TM polarized waves.

## 2.1.2 Propagation Length and Penetration Depth

Absorption, which was not consider until this moment, is not neglectable. These losses are introduced into the equations via a positive imaginary part of metals' permittivity. From equation 2.18 it is possible to introduce an imaginary part to the dielectric constant that will lead to a  $\beta$  with both real and imaginary parts. So it becomes  $\beta = \beta' + i\beta''$ , which allows to define the propagation length. This is the length at which the energy decreases by  $1/e$  of the initial energy ([20]):

$$L = \frac{1}{2\beta''} = \frac{1}{2\Im\left(\frac{\omega}{c} \sqrt{\frac{\epsilon_{metal} \epsilon_{dielectric}}{\epsilon_{metal} + \epsilon_{dielectric}}}\right)} . \quad (2.19)$$

The typical values for the propagation length for gold /dielectric (n=1.32) interface goes from several nanometers for a wavelength of 525 nm up to 100 micrometers for a wavelength of 900 nm ([12]).

A similar concept but along the z-axis is given by the evanescent wave. The penetration depth defines how long will propagate in the z direction until it drops by  $1/e$  of its initial amplitude. Therefore, this characteristic of the system allows for the better preparation of an immunoassay in terms of a layer depth. Analogous from what happened to the propagation length, we have a real and an imaginary wave vector along z-axis. Considering the equations for the electric and magnetic field we can see that the evanescent decay length (penetration depth) is given by:

$$L_{metal} = \frac{1}{\Re(k_{metal})} , \quad (2.20a)$$

$$L_{dielectric} = \frac{1}{\Re(k_{dielectric})} . \quad (2.20b)$$

Considering that wave equation for a transverse magnetic mode is given by:

$$\frac{\partial^2 H_y}{\partial z^2} + \left(\frac{w^2}{c^2}\epsilon - \beta^2\right)H_y = 0 , \quad (2.21)$$

which combined with equation 2.17 results in:

$$k_{metal}^2 = \beta^2 - \frac{w^2}{c^2}\epsilon_{metal}^2 , \quad (2.22a)$$

$$k_{dielectric}^2 = \beta^2 - \frac{w^2}{c^2}\epsilon_{dielectric}^2 . \quad (2.22b)$$

Finally, the penetration depth for both media:

$$L_{metal} = \frac{1}{\Re\left(\sqrt{\beta^2 - \frac{w^2}{c^2}\epsilon_{metal}^2}\right)} , \quad (2.23a)$$

$$L_{dielectric} = \frac{1}{\Re\left(\sqrt{\beta^2 - \frac{w^2}{c^2}\epsilon_{dielectric}^2}\right)} . \quad (2.23b)$$

For a gold/dielectric interface the penetration depth into dielectric is in the  $10^2$  nm order of magnitude. As for the metal, it is more narrow with a 20 to 30 nm penetration depth ([12]).

### 2.1.3 Surface Plasmons Excitation Configurations

The dispersion relationship for the surface plasmons is given by

$$k = \beta = \frac{\omega}{c} \sqrt{\frac{\epsilon_{metal}\epsilon_{dielectric}}{\epsilon_{metal} + \epsilon_{dielectric}}} . \quad (2.24)$$

Comparing this equation with the dispersion relation for photons and considering only the dielectric

$$k_{photon,air} = \frac{\omega}{c} \sqrt{\epsilon_d} , \quad (2.25)$$

it is clear that besides the zero frequency there is not another point where the right momentum and energy conservation can be achieved, as presented in figure 2.3. If a prism is introduced i.e. a high refractive index material, it causes an increase on the refractive index and a reduction on the slope of the dispersion relation of the photons, therefore by rotating the interface one can move along the intersection  $\omega_{laser}$  and  $k_{surface\ plasmon}$  and meet the  $k_{photon, prism}$ . When the three of them intersect, the energy and momentum of plasmon and photon are the same and the surface plasmon excitation is possible to occur.

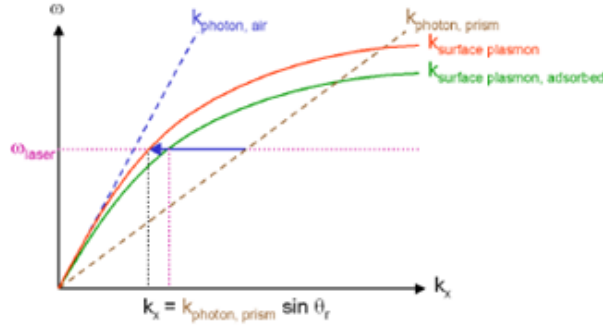


**Figure 2.3:** Dispersion relations for the different apparatus. Figure from [22].

There are two configurations purposed using the prism coupling (Fig. 2.4):

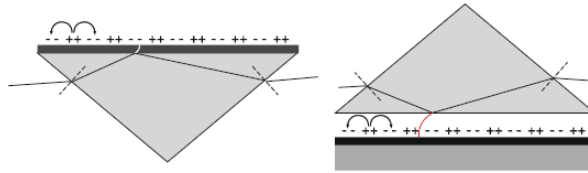


**Figure 2.4:** Surface plasmon polaritons excitation with Kretschmann (left) and Otto (right) configuration. Figure from [20].

The Otto configuration, on the right, has a prism that adjacent to the base has a gap of low refractive index with a thickness of the order of the laser wavelength. On the other side of the dielectric, there is an optical infinite metal layer. After achieving the total internal reflection, the evanescent field can tunnel across the dielectric space and originate surface plasmon modes on dielectric/metal interface. The reflected energy is monitored and the coupling is identified by a minimum on the reflected intensity. However, this configuration presents some drawbacks: the tunnelling process is very sensitive to changes on the thickness of the gap therefore a highly precise thickness must be projected. On the other hand, for binding studies it is necessary to have access to the dielectric layer that keeps the layer thickness which demands a really thin construction that can be build and re-build ([22]). The second approach to a prism coupling was designed by Kretschmann in 1968 ([15]) and it is more robust and relatively simple ([22]). In this configuration the metal layer and the dielectric layer exchange positions as presented on the left side of figure 2.4. The precision in terms of the layer adjacent to the prism base is still important to perform better as we can see from the extreme cases presented in figure 2.5.

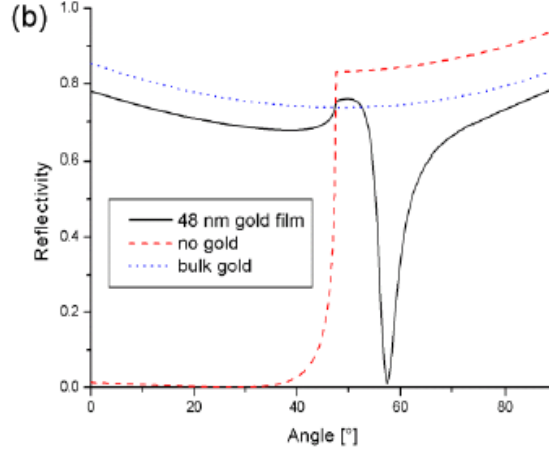


**Figure 2.5:** Reflectivity variation according to the gold layer thickness. Figure from [22].

In this configuration, photons from a beam directed in an angle greater than the critical angle tunnel through the metal film and excite the surface plasmons at the dielectric/metal interface. Another option for the momentum and energy matching are metallic gratings.

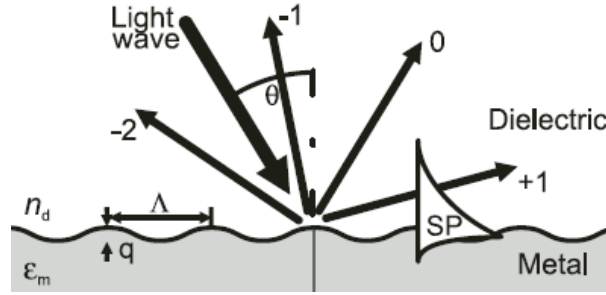


**Figure 2.6:** Grating coupling scheme. Figure from [12].

A grating is a periodic surface modulation with a period  $\Lambda$  that allows for the plasmons excitation when:

$$\frac{\omega}{c} \sqrt{\frac{\epsilon_{metal} \epsilon_{dielectric}}{\epsilon_{metal} + \epsilon_{dielectric}}} = \frac{\omega}{c} \sin(\theta) \pm \nu \frac{2\pi}{\Lambda} . \quad (2.26)$$

where  $\nu$  is the diffraction order,  $\theta$  is the incidence angle, and  $\omega$  is the angular frequency. When the propagation constant of the diffracted wave propagating along the surface (x-axis) equals the surface plasmon propagation constant ( $\beta$ ), a surface plasmon is created.

#### 2.1.4 Why do we need a new diffraction grating?

Surface plasmon resonance based sensors are an optical sensing configuration that is applied for several purposes: medical diagnostics, food safety, process control, environmental monitoring, or even defence issues. Hence, there is not one optimal configuration for all these applications but one configuration may fit best for process control and others for food safety and so on. Therefore, to use effectively a diffraction grating in an optical or an electronic system it urges to understand how grating parameters affect the the quality of the grating for the desired application. Hence, a wavelength, period or other parameter associated with the grating must be optimized, in our case, to obtain higher sensitivities and contrasts.

In this thesis, we will simulate a grating using PCGrate 6.1 for a fixed wavelength in the beginning and a more larger phase space in a second stage.

## 2.2 PCGrate

PCGrate-S(X) 6.1 is a software that is designed to model efficiency of both relief, phase diffraction gratings and rough mirrors. This software can simulate scattering effects on periodic and non-periodic structures using multilayer with micro and nano roughnesss with different shapes. It allows for the simulation of several polarizations (Transverse Magnetic, Transverse Electric and with different angles between TM and TE) with finite (or perfect) conductive or lossless layers. Border profiles can be either user customized with a *.gpp* file or with a predefined shape: trapezoidal, sine trapezoidal, polygonal, trigonometric and section dependent. The program encompasses wavelengths from the X-Rays to the microwave region and uses plane, cylindrical, spherical, and gaussian shaped waves as incident waves using a modified boundary integral equation method to calculate the diffracted wave. The demonstration version allows to simulate three layers with up to 100 points per boundary. There is also a thickness to period ratio limitation: 0.25 thus there are depths that cannot be simulated.

This thesis uses two editions of PCGrate 6.1. Until the first iteration the demo version is used and the produced grating was mainly a result from this version. Moreover, the version was replaced and a larger phase space was used to simulate new gratings. The goal was to cover a large phase to find at least a local minimum that would fulfil our requirements. Once the wavelength and the grating period are defined, the border profile must be decided. Edgy gratings with a triangular or a rectangular shape are not possible to built so only the sine trapezoidal profile was considered (Fig. 2.7) because it is the shape that is possible to manufacture.

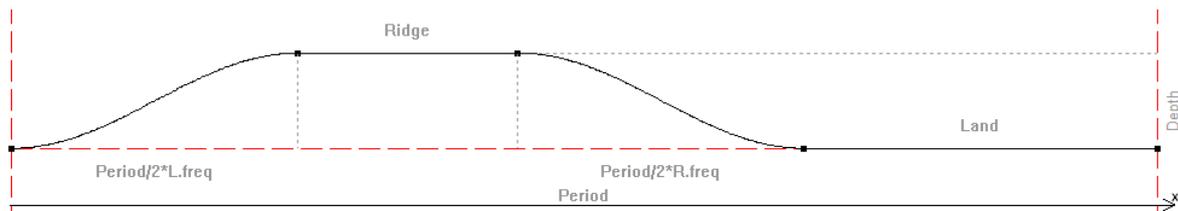


**Figure 2.7:** Sine trapezoidal grating profile from PCGrate 6.1.

In this profile, one can set six different dimensions: period, ridge, land, depth, left frequency and right frequency. Ridge is defined as the width of the plateau at the maximum height and land is the width of the plateau with the height equal to 0 nm. The depth defines the height of the grating profile. Finally, left and right frequency control how steep is the transition from land to ridge. A higher frequency means a more steep transition because the width (in the x axis) of the transition is given by  $\frac{Period}{2F_{req}}$  for each side of ridge and land.

A system to be robust does not need to use only new and very complicated hardware and software. For example, a reading system that works well is the DVD player pickup which uses a disc and reads with a small, fully tested, and approved pickup with a 650 nm diode laser and a numerical aperture of 0.6

which means that for air  $\theta \approx 37^\circ$  is obtained. First, a grating with a fixed wavelength is simulated for different periods. The land is the dependent variable, which is obtained by using the following formula  $Land = Period - Ridge - \frac{Period}{2RFreq} - \frac{Period}{2LFreq}$ .

## 2.3 Results

Results concerning the initial selection are present in appendix. The new solution will use a diffraction grating that instead of needing a large incidence angle would need an incidence angle within  $10^\circ$  so it can contain all the angle variations without losses and would allow for the application of new algorithms. For a fixed wavelength of 650 nm, five periods were tested: 600 nm, 700 nm, 800 nm, 900 nm, and 1000 nm. For each period, the depth was tested and in case the  $\theta_{SPR}$  was less than  $10^\circ$ , both frequency and ridge were simulated. The procedure, initially, was based on the contrast and  $\theta_{SPR}$ . Hence, for a fixed wavelength and for each period the depth, frequency, and ridge are changed and the configuration with the best contrast and  $\theta_{SPR}$  are considered. The three final grating are presented in appendix due to copyrights agreement.

To select which grating was the best, simulations changing the bulk refractive index were performed simulating variations from  $n=1.333$  to  $n=1.4$ . This variation represents the change from an aqueous buffer solution to a solution with a high concentration of proteins ( $n=1.54$ ). The change in the angle of resonance is considered and normalized to reference at  $n=1.333$  for the different gratings. For a surface plasmon resonance based sensor it is important to be sensitivity for surface changes and not to bulk changes, therefore the following simulation taking into account a change in the refractive index was considered: a change from a bulk configuration to a 20 nm layer with a refractive index of  $n=1.4 + i0.2$ . A SPR signal change is measured in terms of the angle shift so a sensitivity metric is the surface sensitivity divided by the bulk sensitivity, that we named as the Overall Sensitivity:

$$OS := \frac{SurfaceSensitivity}{BulkSensitivity} = \frac{|\theta_{SPR} n = 1.333 - \theta_{SPR} n = 1.4 + i0.2|}{|\theta_{SPR} n = 1.333 - \theta_{SPR} n = 1.4|}. \quad (2.27)$$

This way, a higher surface sensitivity and a lower bulk sensitivity reveals a higher overall sensitivity therefore a better grating. Figure 2.8 shows the representation of this coefficient (*y axis*) for the three final gratings (*x axis*). Figure 2.8 shows that when using a wavelength of 650 nm both 800 nm and 1000 nm gratings perform better with a coefficient of 0.51 and 0.54 (5.8 % higher), respectively. In addition to the shift analysis, the signal quality should be considered because the factor does not take into account the dispersion or the contrast associated with the signal. The signal quality factor is expressed in terms of the contrast and the full width half maximum (FWHM). Therefore, a larger contrast will increase the signal quality and a larger FWHM will decrease it so a term given by  $\frac{Contrast}{FWHM}$  of the surface signal is considered since this is the signal that we want to measure and identify. The Overall Sensitivity Corrected is defined as:

$$OSC := \frac{|\theta_{SPR} n = 1.333 - \theta_{SPR} n = 1.4 + i0.2|}{|\theta_{SPR} n = 1.333 - \theta_{SPR} n = 1.4|} \times \frac{Contrast}{FWHM}. \quad (2.28)$$

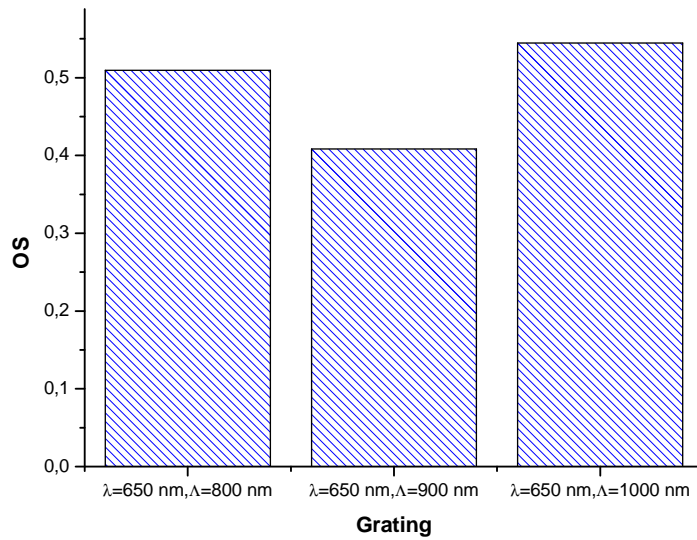


**Figure 2.8:** OS for the different gratings.

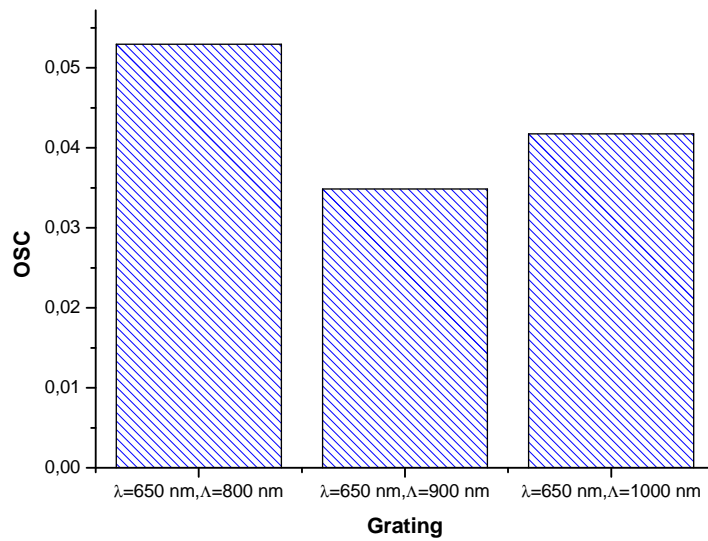


**Figure 2.9:** OSC for the different gratings.

Figure 2.9 shows that there is 27% higher sensitivity for the grating with  $\Lambda=800 \text{ nm}$  compared to the grating with  $\Lambda=1000 \text{ nm}$ . Hence, the grating with a period of 800 nm is selected to be manufactured. As the initial grating was already ordered back in March, further simulations were considered using different wavelengths and more periods. The conditions for a better construction were defined so there was a margin from the desired values and the construction limits. The specifications for the simulations are presented on table 2.1.

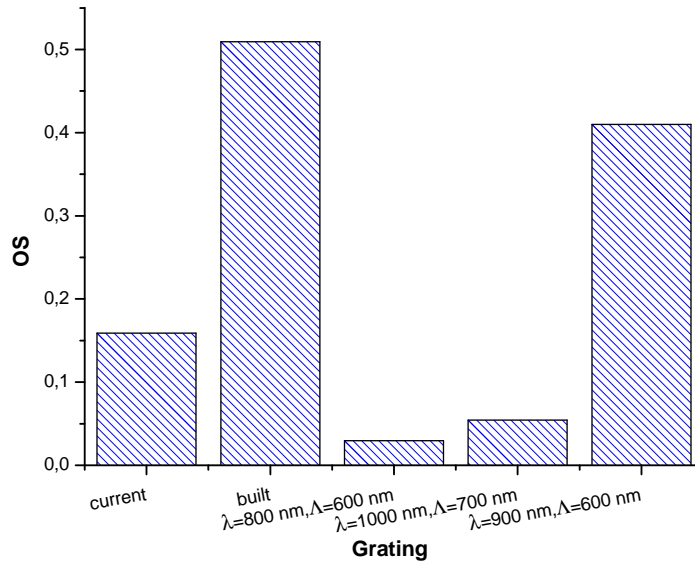
Considering the working restrictions and since it is not manageable to cover all the phase space with a nm step, reasonable steps were chosen for each dimension based on the range of each one. To get, at least,

Characteristic	Minimum	Maximum
Angle ( $^{\circ}$ )	0	10
Wavelength (nm)	400	1000
Period (nm)	600	1600
Depth (nm)	20	100
Ridge (nm)	$\geq 20\%$ Period	
Land (nm)	$\geq 20\%$ Period	
Gold depth	100	100

**Table 2.1:** Grating simulation specifications for the sine trapezoidal grating profile.

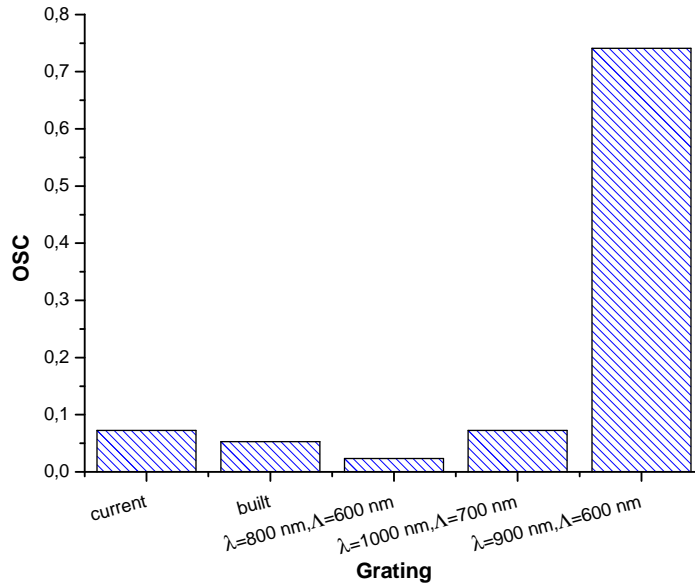
a local minimum the optimization was made for each grating period: 600 nm to 1600 nm with steps of 100 nm. The initial conditions for each grating are the ones with the minimum value for each dimension so the depth is 30 nm, the ridge is 20% of the period, the frequency is 2. To start, the wavelength is incremented from 400 nm to 1000 nm in 100 nm steps. Next, the depth varies from 30 nm to 100 nm with 15 nm steps. Third, the frequency is changed from 2 to 5 with a step of 1 since both 1 and 6 originate a ridge and land that do not meet the requirements. Finally, the ridge varies from the minimum to the value at which the land is less than 20% of the period which is dependent on the frequency. The method to evaluate the sensitivity of the new grating is the same used previously. The sensitivity is, one more time, calculated for the gratings that presented a higher contrast and a resonance angle within the  $10^{\circ}$  range. Summarizing, the final four gratings considered to compare with the current grating are presented in appendix due to copyrights agreement.

Figure 2.10 shows the overall sensitivity not considering the signal quality factor for the four gratings presented on the list and for the current grating used by Biosurfit. We can see that, there is a higher



**Figure 2.10:** OS for the different gratings not considering signal quality effects.

sensitivity for the grating that was built (OS=0.51) and for a grating using a incident wave of 900 nm and a period of 600 nm (OS=0.41). In addition, using just the information concerning the angular shift might hide information about the signal so the OSC is presented for these five gratings in figure 2.11 Adding the



**Figure 2.11:** OSC for the different gratings.

signal quality to the performance metric we can see that the OSC for the built grating is lower than the other three cases since it leads to a higher decrease on the sensitivity. This was expectable because the FWHM of this grating was intend to be higher to allow to calculate area variations. On the other hand, the grating with  $\Lambda=600 \text{ nm}$   $\lambda=900 \text{ nm}$  shows an amplification of 81% in the sensitivity measure due to the signal quality. This is mainly due to the higher contrast (25% higher than the current grating) and a FWHM that does not increases more than  $2^\circ$  while in the rest of the cases it is higher than  $2^\circ$  reaching  $4^\circ$  to  $5^\circ$ , in some cases. The values show that the built grating (OSC=0.05) has a sensitivity 27% lower than the current (OSC=0.07) one. And the grating with a  $\Lambda=600 \text{ nm}$   $\lambda=900 \text{ nm}$  shows a higher sensitivity (OSC=0.74).

## 2.4 Produced Grating

The grating was manufactured by *Synchronicity Mastering Services* and it was characterized using atomic force microscopy (AFM) at Instituto Superior Técnico (IST) with professor Pedro Brogueira and analysed with Nanoscope V6.14r1. The AFM parameters can be found in the appendix. Figure 2.12 presents the groove profile that results from the height channel (Channel 1). This image is obtained after a flatten operation (Analyze->Flatten->Execute) which recovers the height pattern from the original image. The brighter areas represent the ridges and the brownish areas the lands. Figure 2.14 represents an isometric view of the grating. To evaluate whether the characteristic dimensions (ridge, land, depth) are correct, they were measured using Nanoscope V6.14r1. Since the depth could vary, two gratings with the same ridge (115 nm), land (439 nm), and different depth: one with 40 nm and other with 50 nm were ordered. The grating with depth equal to 40 nm analysis is represented in appendix.

The difference between the expected period and the manufactured is less than one sigma for both spindles with less than 1% deviation from the designed value. The ridge and the land have opposite

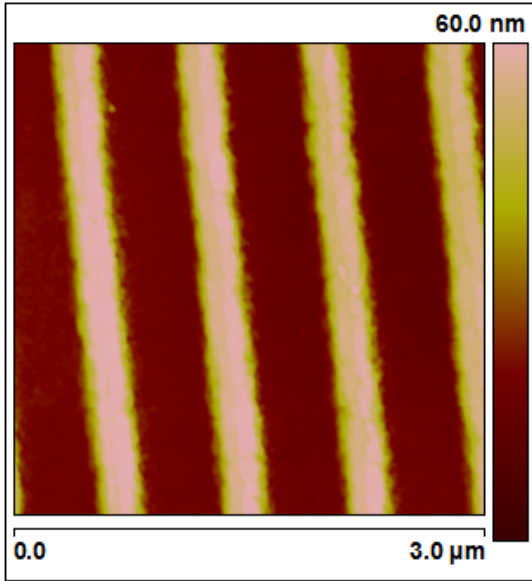


**Figure 2.12:** Depth profile through AFM analysis.

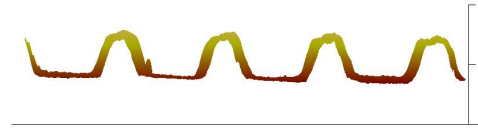


**Figure 2.13:** Front view of the grating.

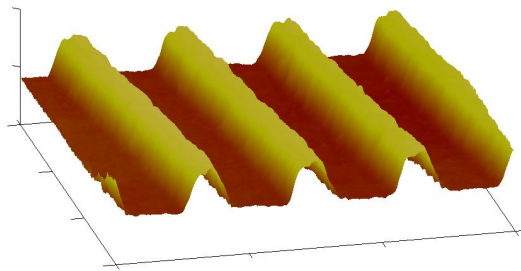


**Figure 2.14:** Isometric view of the grating.

deviations (one is larger and the other lower) from the expected values which is comprehensible since the transitions ridge-land and land-ridge are similar and the period is more or less the expected. The differences in these two cases vary from  $+8.2\%$   $+12.5\%$  for the ridge and  $-2.4\%$  to  $-5.2\%$  for the land which considering the error corresponds to not more than two sigma. Last, the depth presents an error that can represent up to  $10.7\%$  of its nominal value which leads to less than one error deviation from the intended value. The grating with depth equal to  $40\text{ nm}$  analysis is represented in appendix.

Table with the AFM results in appendix shows the AFM results for the grating with  $\text{depth}=50\text{ nm}$ . The difference between the expected period and the manufactured is at maximum  $1.13$  sigma for both spindles with less than  $2\%$  deviation from the designed value. The ridge and the land have opposite deviations for the same reasons explained before. The ridge presents no more than  $1.22$  sigma from the desired value while the does not reach the  $0.5$  sigma deviation. Finally, the depth presents a smaller error which lead to more than two error deviations from the intended value.

## Final Remarks

Overall, the produced grating is within the expected range of deviation accepted (10%) so the final result from *Synchronicity Mastering Services* can be used to further investigation with a new setup. Even though, we presented here the selection and the evaluation of this new grating profile, there were problems regarding its manufacturing. The grating was predicted to be ready by the middle of April allowing the tests during the following months but due to a misleading on the dimensions and on the stamper to use, it resulted in a delay of four months that interrupt the construction of the new setup. Despite this bottleneck, we decided to continue with the magnetic nanoparticle project using the existing detection setup and select the most suitable magnet configuration which will be presented in the following sections.



### 3.1 Immunoassays & SPR

An immunoassay is a test that is used to detect certain molecules using the ability of antibodies to bind to a specific molecule. The classical immunoassays rely on the signal generated by the labels like fluorescent dyes or radioisotopes. The usage of labels has several problems such as undesired interactions between the analyte and the biomolecule used for recognition.

SPR based biosensors use the effect of the biomolecules binding directly as a shift in surface refractive index therefore, if treated correctly, it can overcome the referred problems. There are several appropriate configurations for immunoassays: Direct, Competitive, Inhibition, and Sandwich Assays ([9]).

A direct assay (Fig. 3.1) can be explained by an interaction like  $A + B \rightleftharpoons AB$ . The antibodies are immobilized on the sensor surface so the analytes can bind to it. The solution with the analyte flows over the sensor surface and the amount of the biomolecule that binds will influence the strength of the output signal. Another way of using the SPR principle for immunoassays is through competitive assay

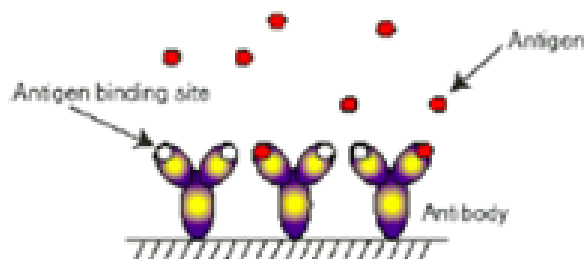


**Figure 3.1:** Direct Assay. Figure from [9].

(Fig. 3.2). This kind of approach is used when the molecular weight of the analyte is low so it does not generate a measurable signal using a direct assay. Analogous to the previous configuration the antibody is immobilized against the sensor surface and a solution with mixed antigen and antigen conjugate is used. The antigen conjugate increases the total molecular weight so it enhances the angle shift associated with the antibody - analyte binding. If the concentration of antigen is lower than the concentration of the conjugated tag, it will have a higher enhancement (less competition) while a higher antigen concentration relative to the conjugated tag will lead to a weaker signal (more competition). An inhibition assay (Fig. 3.3) uses the analyte attached to the sensor surface and the high molecular weight of the antibodies is used for detection. The sample solution is a mixture of antibodies with excess analyte which result in antibodies that bind to both immobilized antigen and in solution analyte. The difference between a

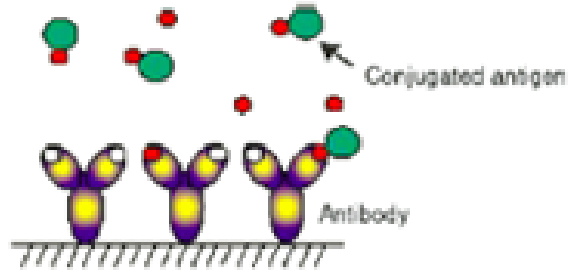


**Figure 3.2:** Competitive Assay. Figure from [9].

sample without antigen and the describe one allows to calculate the amount of antigen in the sample. Higher concentrations of antigen lead to more binding of antibodies therefore less binding to the sensor surface which leads to a lower signal. Finally, in a sandwich assay (Fig. 3.4) a structure with antibody -

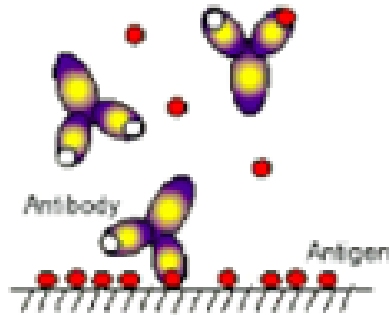


**Figure 3.3:** Inhibition Assay. Figure from [9].

analyte - amplification tag is formed. First, the antibodies are attached to the surface sensor. Next the analyte flows and interacts with the antibody. Last, the amplification tag, such as a secondary antibody or a nanoparticle, flows to increase the signal. To measure the right signal, it is advisable to use high affinity antibodies. A SPR immunoassay can be study with a sensogram that represents the resonance

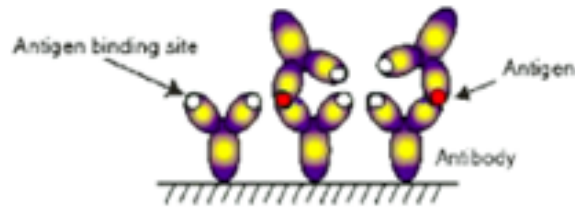


**Figure 3.4:** Sandwich Assay. Figure from [9].

angle as a function of time. Usually, a SPR based immunoassay starts with a base signal that serves as the initial reference (BaseLine 1). This signal will increase with the introduction of the target solution (Association) until the saturation or until a new solution is introduced and then the signal stabilizes (BaseLine 2). In some assays, a dissociation and a regeneration may be present. A further analysis on the kinetics ([13]) related with the association and dissociation phases allows to find the constants that

describe both association and dissociation and can give insights about how effective is the introduction of more analyte.

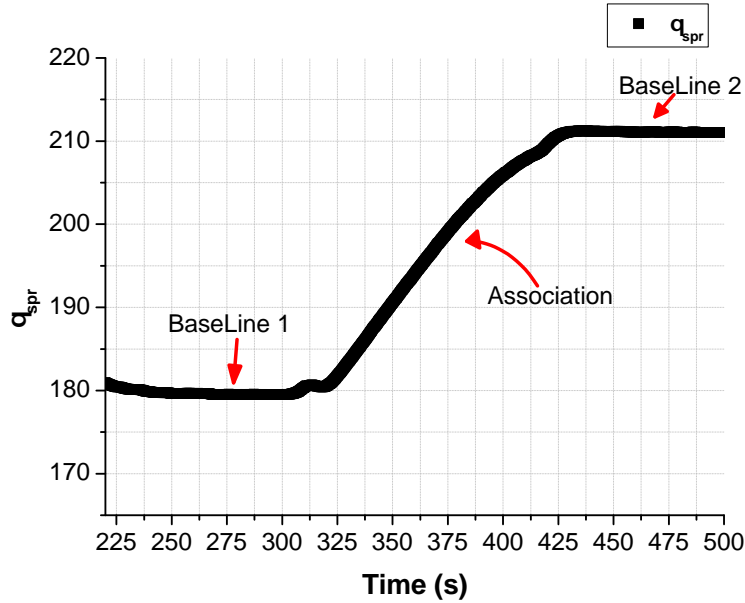


**Figure 3.5:** Example of a sensogram.

The most common model for the rate calculation is the Langmuir model that describes the interaction between one ligand and one analyte.



The model assumes that binding and dissociation reactions are equivalent and independent from binding site to binding site. Furthermore, mass transport limitations are not considered. If the concentration of analyte ( $[A]$ ) is considered constant due to a larger mass transport than the association rate it is possible to write the association rate as

$$R_{association} = \frac{k_a[A]R_{max}}{k_a[A] + k_d} [1 - e^{-(k_a[A]+k_d)t}] , \quad (3.2)$$

where  $k_a$  represent the association constant,  $k_d$  the dissociation constant, and  $R_{max}$  the maximum association that the system can achieve. Studying the dissociation the same constraints are applied but this time it only has the dissociation constant participating so the result is an exponential decay of the response

$$R_{Dissociation} = \frac{k_a[A]R_{max}}{k_a[A] + k_d} e^{-k_d t} . \quad (3.3)$$

Considering equations 3.2 and 3.3 the equilibrium is achieved for:

$$R_{equilibrium} = \frac{k_a[A]R_{max}}{k_a[A] + k_d} , \quad (3.4)$$

from which it is easy to see that if  $k_a [A] \gg k_d$  the system is able to reach the highest value if response possible. In case the dissociation constant is much higher -  $k_a [A] \ll k_d$  - the equilibrium value is

dependent on the association and dissociation constants.

## 3.2 Magnetic Nanoparticles and Magnetic Forces

Magnetic nanoparticles are given more and more attention for lab-on-a-chip applications due to the possibility for in flow manipulation and functionalization with biomolecules. A magnetic nanoparticle is usually formed of magnetic nanocrystals surrounded by a non-magnetic matrix that is bio-compatible. Iron oxides are more stable against oxidation so they are preferable to iron ([10]). MNPs can be formed by superparamagnetic nanocrystals in a polymer matrix that avoids direct contact between the biological element and the metal oxide. These crystals are characterized by randomly oriented magnetic moments in case they are not in the presence of an external magnetic field. When acted by an external magnetic field, all moments are aligned in a preferential direction. Once the magnetic field is switched off, all moments return to the random configuration (Fig. 3.6). This characteristic allow for the resuspension of

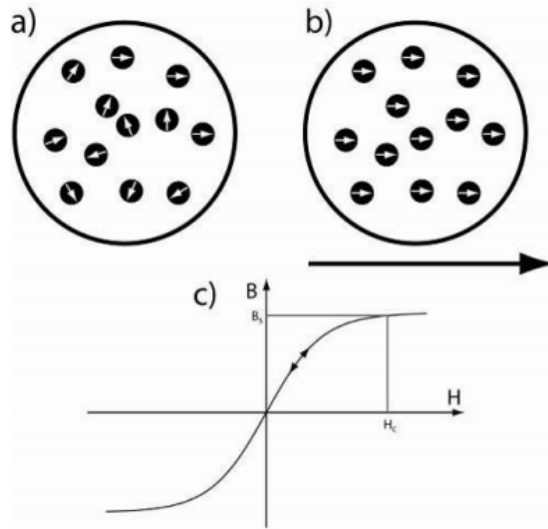


**Figure 3.6:** Magnetic moments behaviour with the external applied field. Figure from [21].

the nanoparticles without agglomeration ([10]), hence the possibilities for switching on and off the field are enormous. Larger nanoparticles with diameters from 0.5  $\mu\text{m}$  to 5  $\mu\text{m}$  have a multi-domain structure and have a hysteresis curve that present a remnant magnetization, resulting in bead clustering therefore for this application smaller nanoparticles are preferable.

The magnetic force acting on a superparamagnetic is not only function of the magnetic field intensity itself. It is important to consider the gradient because an uniform field would give rise to a torque and not to a translational movement. The magnetic force acting on a single superparamagnetic particle with a magnetic moment  $\vec{m}$  and in presence of an applied magnetic field  $\vec{B}$  is given by ([10]):

$$\vec{F}_{mag} = \frac{1}{\mu_0} \nabla \vec{m} \cdot \vec{B} , \quad (3.5)$$

which assuming that the magnetic moment is not varying in space, for example, assuming that the

nanoparticles is at saturation -  $M_{sat}$  the expression can be simplified to

$$\vec{F}_{mag} \approx \frac{1}{\mu_0} (\vec{m} \cdot \nabla \vec{B}) . \quad (3.6)$$

In case the medium in which the nanoparticles are prepared and used is non magnetic, the magnetic moment can be written as

$$\vec{m} = V \mu_0 \vec{M} = V \mu_0 \chi \vec{H} , \quad (3.7)$$

where  $\vec{H}$  is the magnetization and  $\chi$  is the magnetic susceptibility of the particle that using the relation  $\vec{B} = \mu \vec{H}$  gives rise to:

$$\vec{F}_{mag} = \frac{V \chi}{\mu_0} (\vec{B} \cdot \nabla) \vec{B} . \quad (3.8)$$

Assuming that  $[\nabla \times \vec{B}] = 0$  and applying the vector calculation  $\nabla(\vec{B} \cdot \vec{B}) = 2(\vec{B} \cdot \nabla) \vec{B}$  the magnetic force become:

$$\vec{F}_{mag} = \frac{V \chi}{2 \mu_0} \nabla \vec{B}^2 . \quad (3.9)$$

To use these nanoparticles for immunoassays and for manipulation of biological material, they are inserted in a liquid flow with some viscosity associated with it. Therefore, the magnetic force has to be larger than the drag force to effectively pull and push the nanoparticles. In this setup, there are four important forces: drag , magnetic , buoyancy and gravity ([21]). Due to the small size of the nanoparticles, both gravity and buoyancy are neglected and the magnetic force has only to compensate the drag force to act in an effective way. The drag force is dependent on the Reynold's number ( $Re$ ) which accounts for the flow conditions, the size of the nanoparticle ( $r$ ), the viscosity of the media ( $\eta$ ), and the velocity of the bead with respect to the containing media ( $\Delta \vec{v}$ ) ([21]):

$$\vec{F}_{drag} = 6 \pi \eta r \Delta \vec{v} . \quad (3.10)$$

## 3.3 Material

### 3.3.1 Spinit<sup>®</sup>

Spinit<sup>®</sup> is a device that is able to perform cell type and immunoassay clinical tests and includes a considerable amount of the most common blood analysis. The device can be divided into the reader and the cartridges. The basic specifications show that the user friendliness is not only about the software and the display but also the weight and the size :

- Size: 31x25x20 (cm)
- Weight: 3.6 kg
- Temperature Control Precision: 0.1°C
- Main Board: Mini-ITX x86
- IDE: OS + Proprietary Data Analysis Software

- Connectivity: Ethernet + USB ports

Spinit<sup>®</sup> is constituted by a multi-function electronic board that has the systems to control the temperature, various sensors, optical modules, and a CD drive control (rotational speed). This CD can be controlled with an approximate 10 micrometre scale precision.

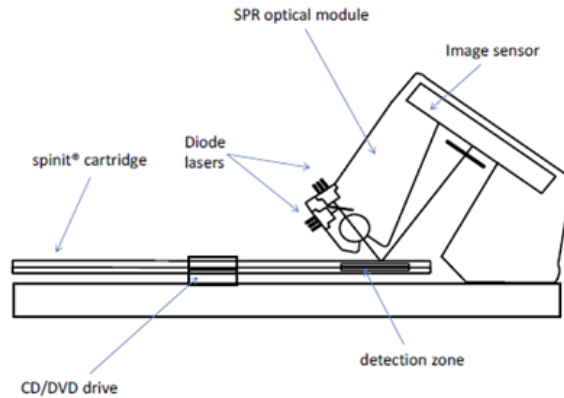


**Figure 3.7:** SPR module and cartridge. Figure from [2].

## SPR Module

The SPR detection system uses a microfluidic "lab on a disk" substrate with a controlled rotation. The reader comprises an optical module with a light source and a detector to receive the signal from the substrate. While the disk is rotating the detection module receives light from the substrate and stores the intensity profile. As Spinit<sup>®</sup> cartridges use detection zones, the data is collected while the detection zones pass in the detection window. Thus, a proper alignment mechanism is needed. The triggering mechanism is presented in appendix. The first part of the data handling cares about capturing the references (S1), that is capture the signal before any analyte-antianalyte interaction. Next the same signal is captured for the assay (S2). The final result is a division  $S2/S1$  because that way the relative intensity is presented and the SPR deep can be calculated.

## Discs

In addition, a microfluidic platform, that allows for the liquid sequencing, is needed, to perform the several steps in an immunoassay. The microfluidic channel system was developed at Biosurfit considering the optimization of solution volume and amount of liquids to be sequenced (Patent US20140109972 A1). The polycarbonate discs are manufactured by Axxicon and have a 120 mm diameter and are 600  $\mu\text{m}$  thick. The microfluidic disc and the working principle are presented in appendix. The first liquid zone must be filled with 25  $\mu\text{l}$  of solution and the following eight chambers with 20  $\mu\text{l}$ . These discs were mastered by Ritek and were then milled with a computer numerical control (CNC) in which the beginning of each zone was drilled with 500  $\mu\text{m}$  drill to create the liquid inlet. The procedure to use the CNC machine can be found in appendix. Besides the nine liquid holes, a tenth was created to work as air outle. After the milling process, the grating discs were cleaned with a air duster gun and stored in a disc box with

capacity for 25 discs using spacers.

In addition, to the microfluidic disc, a grating disc is needed. The grating disc is a polycarbonated disc with a costumed grating profile that is optimized for SPR detection. This disc is molded by Ritek and has a 120mm diameter and is 600  $\mu\text{m}$  thick. It is sputtered at Biosurfit which creates 12 gold spots. The third component of the disc is the dry-film photopolymer which is 20  $\mu\text{m}$  deep. To define the detection zones the dry film is cut in so only the detection zones are dry-film free. The cut profile is presented on figure 3.8.

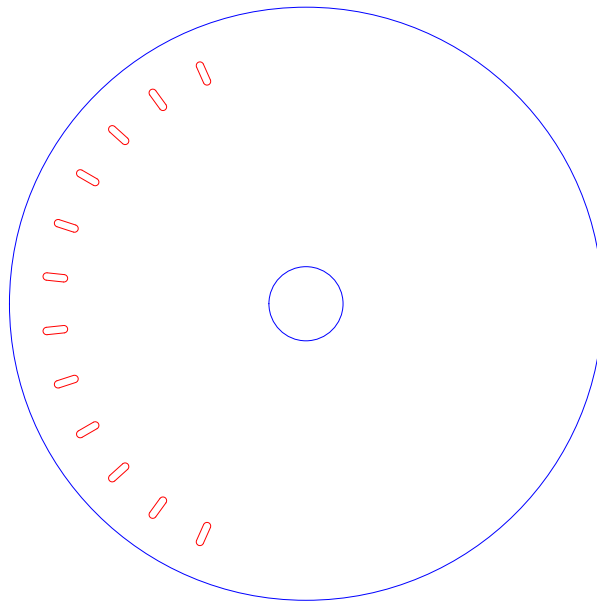


**Figure 3.8:** Dry-film cut profile.

After these three stages are completed, the assembling takes place. The assembling process is explained in appendix.

### 3.3.2 Working Solutions

An immunoassay in these discs is completed after the passage of several liquids. The solutions that were used in the final version of the immunoassay are the following:

- Phosphate buffer saline (pbs),
- Biotinylated bovine serum albumin (bsa-bt),
- Streptavidin+Thiol,
- Magnetic nanoparticles (MNPs),
- Blocking,

- Surfynol .

The pbs solution contains 10 mM phosphate buffer, 137 mM sodium chloride, and 2.7 mM potassium chloride tablets are produced by AMRESCO (tabs #E404-200 tabs lot #2223c318). These tablets were mixed into 100 ml of ultra pure water with a magnetic stirrer that resulted in PBS 1X with a pH on average of 7.4 and was stored in a fridge. This solution was used both as a buffer to calculate the baselines and as a dilution for the other solutions.

The blocking solution consisting of low-molecular weight casein fragments with sodium chloride and tween allows for the saturation of the binding capacities on plastic consumables so the non specific binding can be reduced. The efficiency of the solution provided by *Candor* is improved due to the production of casein with different molecular weights. This solution has a  $pH = 7.2 \pm 0.2$ . Streptavidin+thiol from protein Mads (Cat#SVT LOT#1306SVT2) is provided at  $1 \text{ mg ml}^{-1}$  in citrate buffer (pH=4.5) and with EDTA ( 3 mM ) as preservative.

The bsa-bt is bought from Sigma (cat# A8549-10mg Lot#SLBC 7388V arrived 23th August 2013 stored at  $4^{\circ}\text{C}$ ) and comes in form of powder. Has a purity of at least 80% and 10 ml of  $H_2O$  were added to the vial and the powder dissolved through inversion. All protein was aliquoted under flame in landing tubes, 500  $\mu\text{l}$  each, in a total of 20 tubes.

The projected discs need that the first liquid overcomes the syphon by capillary action so the adherence to the channels must be assured. This way, the surface functionalization is assured with a dilution in a surfynol solution. The surfynol 0.5% is formed using 10  $\mu\text{l}$  of surfynol 465 from Air Products with 1990  $\mu\text{l}$  of pbs 1X obtained as described previously. This surfactant allows for a "low foam surface tension reduction with improved solubility and compatibility in waterborne coatings, inks, and adhesives systems". Next, the streptavidin+ thiol with a concentration of  $1 \text{ mg ml}^{-1}$  is diluted into the surfynol solution to generate the final solution.

The immunoassay that we intend to perform was based on the very high effective binding of streptavidin and biotin therefore magnetic nanoparticles coated with streptavidin were used since each bsa had five biotins to attach to streptavidin and therefore a higher probability of interaction. Micromod's nanoparticles shaped as clusters with diameters of 20 nm, 50 nm, and 100 nm were bought with an iron concentration of  $2.4 \text{ mg ml}^{-1}$  and a density of  $1.4 \text{ g cm}^{-3}$ . They were stored in a solution with a pH of 7.4. Chemicell also provided nanoparticles dispersed in a 7.4 pH solution with a density of  $1.25 \text{ g cm}^{-3}$ . Two different diameters were available: 100 nm and 200 nm . Admetech streptavidin coated nanoparticles are available in four different diameters 100 nm, 200 nm, 300 nm and 500 nm. They present a density of  $2 \text{ g cm}^{-3}$  and a binding capacity of  $4490 \text{ pmol mg}^{-1}$  while Chemicell's nanoparticles present a  $80 \text{ pmol mg}^{-1}$  and Microdmod's approximately  $30 \text{ pmol mg}^{-1}$ .

### 3.3.3 Magnet & Magnet Holder Prototype

An immunoassay with magnetic nanoparticles requires a nouvelle setup to handle the magnets that will create the magnetic field and allow the actuation on the MNPs. Magnets used in these experiments were bought from *Neotexx*. Neodymium boron iron (NdFeB) magnets with a nominal  $B_r$  of 1.33 T.

*Neotex* magnets showed actuation forces up to 20 pN which is coherent with the values calculated by other studies as the necessary retention force ([24]). Electromagnets from *RS* and the MidiMACS<sup>®</sup> from *MiltenyiBiotec* were used to test the possibility for a different implementation. Three different electromagnets were ordered with a diameter of 20 mm, 25 mm, and 30 mm with retention forces up to 53 N. MidiMACS<sup>®</sup> was tested because is indicated for cell separation in columns.

As Spinit<sup>®</sup> encompasses both the driver and the detection system for the SPR signal there were obvious limitations with respect to the mounting of the new prototype. The magnet handler was designed to optimize the number of magnets to use and to be implemented without fundamental changes on both drive and sensing system. The result of several iterations using the Solid Works Premium 2009 and a 3D printer (Makerbot Replicator 2 Desktop) is the design on figure 3.9. From figure 3.9 and figure 3.10 it is

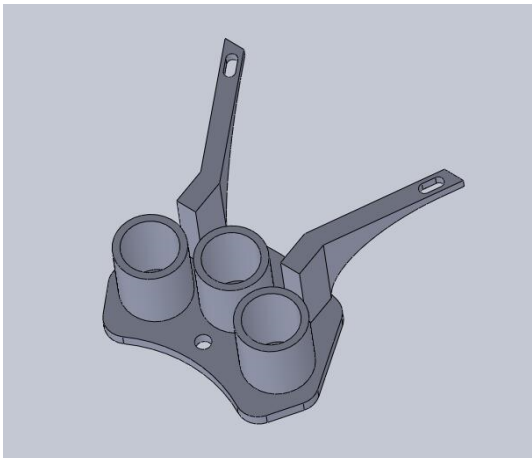


**Figure 3.9:** Magnet holder prototype with three pieces connected.

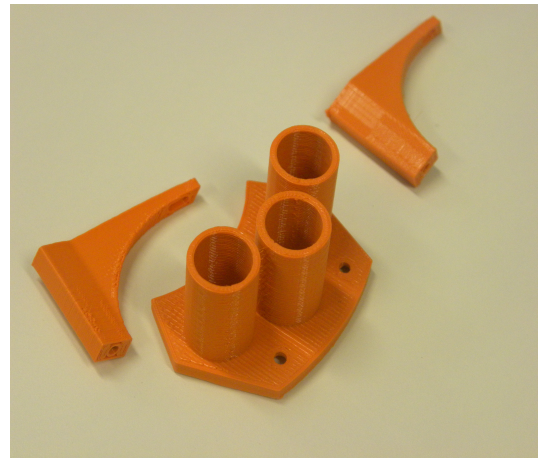


**Figure 3.10:** Magnet holder prototype built with a 3D printer.

clear that the base in which the magnet will be supported does not have spiky edges so there are not problems with wires that get damaged due to the edges. On other hand, the extensions with holes in the edge allow that it can be implemented without any change in the drive using only screws already available on the drive.

This support allows for the allocation of three magnets near the sensing surface and near the syphon which is expected to increase the retention capacity not only on the detection zone but also starting on the syphon area. Considerations about the magnet shielding were not taken into account at this point because, after one month, differences on the electronic systems were not observed.

### Shift Calculation

A SPR immunoassay is evaluated based on the difference in terms of resonance angle due to the presence of a ligand. The result of an experiment is a sensogram (Fig. 3.11) that is a plot that represents the  $\theta_{SPR}$  in time, therefore it allows us to see the dynamics of the reaction. Typically there is an initial washing with a buffer solution that allows to set the initial  $\theta_{SPR}$  value. Next, the intended analyte with or without an amplification tag flows over the sensor surface and interacts with the functionalized surface leading to an adsorption that shifts the SPR angle. To evaluate the actual angular shift the reference solution is passed first so the difference can be associated to the interaction between the target analyte

and the sensor surface functionalization. The adsorption dynamics is characterized by an initial high rate association between the analyte and the surface which is mainly due to the amount of available association sites. As these sites are being fulfilled the rate decreases and finally the last wash leads to a decrease that will reach an equilibrium between the association and dissociation. As this difference between the initial and the final wash are essential to measure the interaction, it is important to develop a systematic method to calculate each baseline: before and after the analyte/amplification stage.

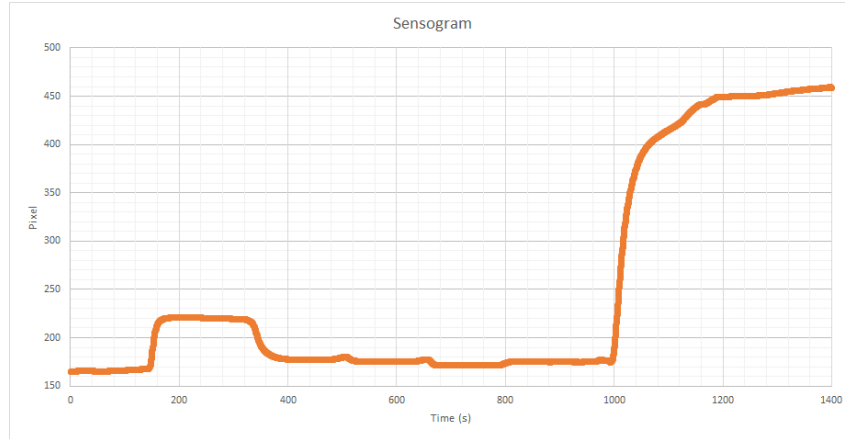


**Figure 3.11:** A sensogram resulting from a sandwich immunoassay using streptavidin+thiol on the surface, bsa-bt as analyte and 120 nm magnetic nanoparticles as amplification tags.

The original data comes in a .txt file with a time step that varies from 0.1 seconds to 0.3 seconds and each liquid passes through the detection zones for 100 seconds up to 300 seconds, so in case there are spikes that are not representative, but only oscillations of the acquisition system, it is important to smooth the data and avoid these spikes. We decided to smooth the data with a simple moving average (SMA) which for each time instant  $t$  takes into account a fixed time window, both to the right and to the left of the instant  $t$ . For example, for a time window of 4 seconds, we consider the interval  $[t - 2 s ; t + 2 s]$ . This procedure is applied to the original data considering a time window of 1, 2, and 4 seconds.

*Smoothed* =

$$\frac{f(t - window/2) + f(t - window/2 + timestep) + \dots + f(t + window/2 - timestep) + f(t + window/2)}{\frac{window}{timestep}} \quad (3.11)$$

Considering the smoothed sensogram, the derivative point by point is calculated and plotted with respect to time:

$$\frac{dSmoothedSensogram}{dt} = \frac{SmoothedSensogram(t_2) - SmoothedSensogram(t_1)}{t_2 - t_1} \quad (3.12)$$

The goal of the described operations is to calculate a proper time reference to obtain both baselines, so the maximum of the derivative is taken to be the reference. As we are taking a derivative from discrete data, the maximum might be a single variation on the area of interest so the calculation takes into account that near the maximum there are more points with a derivative that have a value no less than 95% of

the maximum. The centroid of this region is calculated:

$$D_{Max} := \text{Maximum of derivative} = \frac{\sum_{t_-}^{t_+} \text{Pixel.time}}{\sum_{t_-}^{t_+} \text{Time}}, \quad (3.13)$$

and the time at which the maximum occurs by:

$$t_{max} := \text{Time @ } D_{Max} = \frac{\sum_{t_-}^{t_+} \text{Pixel.time}}{\sum_{t_-}^{t_+} \text{Pixel}}. \quad (3.14)$$

Now that we have the instant at which the adsorption reaches its maximum we can sum and subtract the instants to get the baseline for the initial and final wash. Depending on the speed of the assay, the time needed to reach the equilibrium might vary so an instant  $t_{plus}$  and  $t_{minus}$  are defined for each speed and assay, and added to the instant at which the maximum of the derivative occurs. The baseline is calculated considering a 2 seconds window so the interval for the baseline is  $[t_{max} + t_{minus} - 1; t_{max} + t_{plus} + 1]$ . The same procedure is considered for the lower baseline. There might be some temperature drifts and flow conditions that cause the signal to not stabilize so the data within the interval has to fulfil two conditions:

$$\begin{aligned} \text{Averagederivative}@[t_{max} + t_x - 1; t_{max} + t_x + 1] &< 10\% D_{Max}, \\ \text{StandardDeviation}@[t_{max} + t_x - 1; t_{max} + t_x + 1] &< 1 \text{Pixel}. \end{aligned} \quad (3.15)$$

The first condition guarantees that the data oscillations are small compared to the maximum of the derivative so we can calculate the average on a plateau. To double check system the standard deviation of the interval is calculated and has to be less than a pixel which is the precision of our measurement.

## 3.4 Results

### 3.4.1 Assay Development

The interaction that we will test will be an avidin - biotin binding because its dissociation constant is one of the lowest existing in nature ( $k_d = 1 \times 10^{-15} \text{M}$ ) while the usual values are at least five orders of magnitude higher. Considering that the nanoparticles produced by the different suppliers are functionalized either with biotin or streptavidin, this will be the target interaction.

The main goal of the magnet and magnetic nanoparticles implementation is to serve as an amplification tag of the reaction. After the assembling, we have a microfluidic disc with a bare gold surface which needs to be functionalized to interact with the biological elements. One of the most efficient ways of interacting with gold is to use thiol because of the affinity of the sulfur to the gold surface. This semi-covalent interaction has a strength of  $45 \text{ kcal mol}^{-1}$  ([29]). Other way of getting the surface functionalized is to use the non-specific interaction of the proteins to the surface, for example, the reaction of bsa-bt with the gold surface as used in [6].

This interaction was tested initially with static Spinit<sup>®</sup> setup. This setup used metallized discs with gold spots and channels that allow for the inflow and outflow of the liquids using a peristaltic pump.

The detection system was an open drive with a SPR module that was connected to an ITX board, which allowed for the real time monitoring of the reaction (In appendix). The assay was conducted with a timer that would allow for monitoring each liquid passage, so after a predefined time the peristaltic pump was paused and the tubes changed for the next liquid. The static SpinIt<sup>®</sup> setup allowed for several conclusions regarding the nanoparticles supplier to use, the magnet and the bsa-bt concentration that would lead to the signal saturation.

The experiments with this setup showed that it was not possible to use the magnet from Midimacs or the electromagnets from RS, because they would lead to a visible interaction only after a couple of hours, when it was visible. In addition, it allowed to see that for a nanoparticle solution at  $6 \times 10^{10}$  NP ml<sup>-1</sup> the concentration of bsa-bt at which the streptavidin coated nanoparticles from Ademtech would saturate was 5 µg ml<sup>-1</sup>. Experiments with this setup confirmed that the slower the nanoparticles flow through the detection zone higher the final shift was obtained. To further confirm this results and before using the liquids sequencing discs this assay was implemented on the c-reactive protein discs. These discs were first functionalized with bsa-bt at 30 µg ml<sup>-1</sup> deposited in 20 µl drops with a pipette on the surface and blocked with a blocking solution. Three holes were made in the disc for the reference pbs, MNPs, and for the washing pbs. In these discs, different concentrations of 100 nm diameter nanoparticles coated with streptavidin were tested.

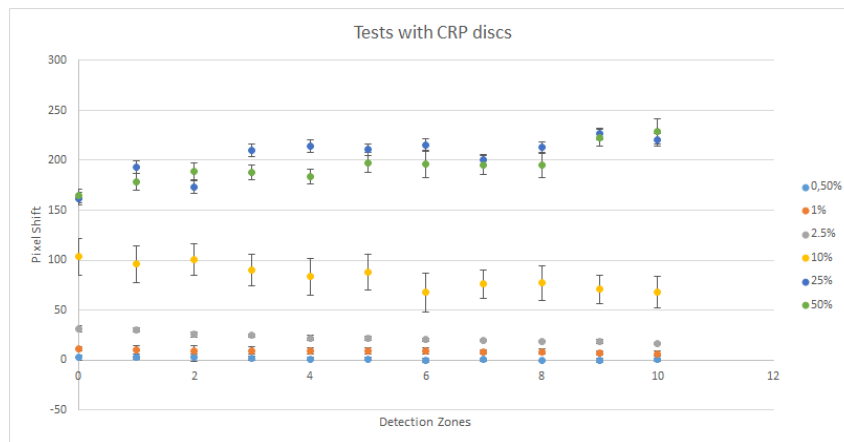


**Figure 3.12:** Test for the interaction between a pre-coated gold surface and 100 nm diameter streptavidin coated mnps from Ademtech.

Figure 3.12 shows that with a 30 µg ml<sup>-1</sup> bsa-bt solution on the sensor surface and 100 nm diameter streptavidin coated nanoparticles, the system saturates at  $6 \times 10^{11}$  NP ml<sup>-1</sup> (25 % of the stock solution) and the detection limit of nanoparticles is approximately a concentration of  $1.4 \times 10^{10}$  NP ml<sup>-1</sup> (0.5 % of the stock solution).

When analysing an assay, it is important to know if the value that is being measured is due to the target interaction or due to some non specific binding (nsb). In this case this might occur between the magnetic nanoparticles and the gold surface, since it is being tested for the case when the surface is blocked and there is no bsa-bt on the surface. These values are not constant for each concentration because as the nanoparticles concentration increases the amount of non specific binding increases, therefore, to fully

characterize an assay, this interaction should be calculated for all the concentrations used. Since this was a preliminary test, it was used as a saturated concentration resulting in approximately 20% NSB for each detection zones. Despite the interaction present values up to 228 pixel shift, the non specific interaction represents a fifth of the nominal value, so a more reliable assay should be implemented with the liquids sequencing discs.

### Liquids Sequencing Discs Experiments

The first experiments with the new discs were concerned about the assay to evaluate the magnetic interaction. Besides the assay with bsa-bt on the surface which interacted with streptavidin coated nanoparticles there was the possibility of creating a sandwich immunoassay with a surface functionalization of streptavidin followed by bsa-bt flows and streptavidin coated nanoparticles.

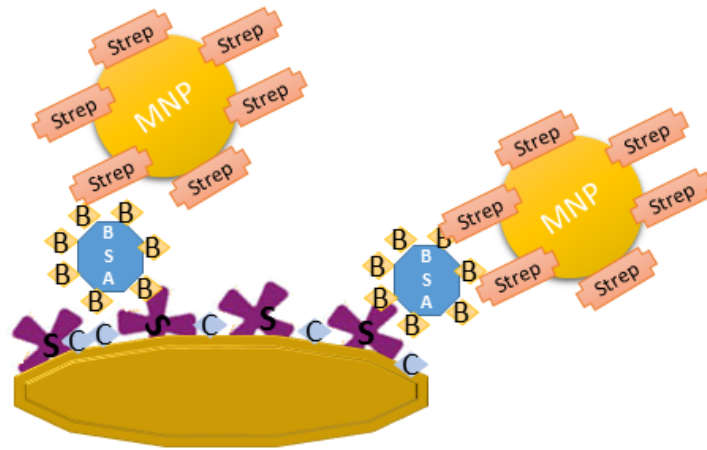
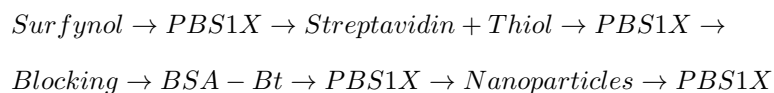


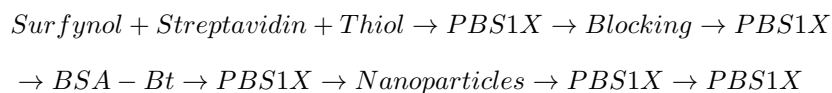
**Figure 3.13:** Diagram of the intended assay.

The decrease on the non specific binding due to the initial surface functionalization with streptavidin led to a non-specific binding of 9 pixel which is five times lower than the assay only with the interaction between nanoparticles and the bsa-bt. Despite the decrease on the nsb, this value is still considered too high.

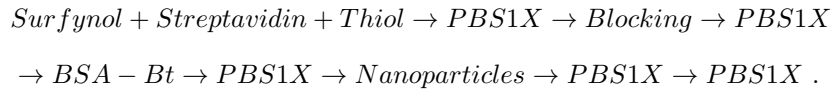
As the discs were used with a surfactant the initial liquid it may connect to surface and decrease the amount of streptavidin that attaches to gold so the comparison using for the first liquid only the surfactant and the surfactant with streptavidin were carried on. To test this effect two assays were performed:



and



The results from this experiment showed that there was a 30% increase (140 pixel to 182 pixel) in terms of shift when using surfynol combined with streptavidin+thiol. Therefore, the final configuration to use for testing with the magnet implementation was the one where the first liquid already contained streptavidin.



Ideally, the result from an assay would be from the interaction between the surface recognition element and the target analyte. But this is not always the case, and, as explained previously, there are unwanted interactions between the amplification tag and some element on the surface leading to a result that is misleading. Therefore, the system is characterized by calculating the non specific binding for different concentrations of nanoparticles. The non specific interaction is measured with an assay in which the target analyte is not used and the nanoparticles can only interact with the surface or with other elements on the surface. In addition, it can be noticed that this value is not the same for all concentrations because as the concentration increases the interaction probability increases leading to higher nsb values. With this assay, we are overestimating the actual value since no analyte is being used and the probability of the interaction between the nanoparticles and the surface is maximized.

Hence, assays in which the nanoparticles flow after the blocking were performed in both Spinit<sup>®</sup>. Figure 3.14 shows the nsb value for all zones. The error is estimated to be the average deviation from the mean. In all these graphs the Spinit<sup>®</sup> with a magnet is named Spinit<sup>®</sup>221 and the regular one as Spinit<sup>®</sup>223. This is due to the numbering of the Spinit<sup>®</sup> on the server.

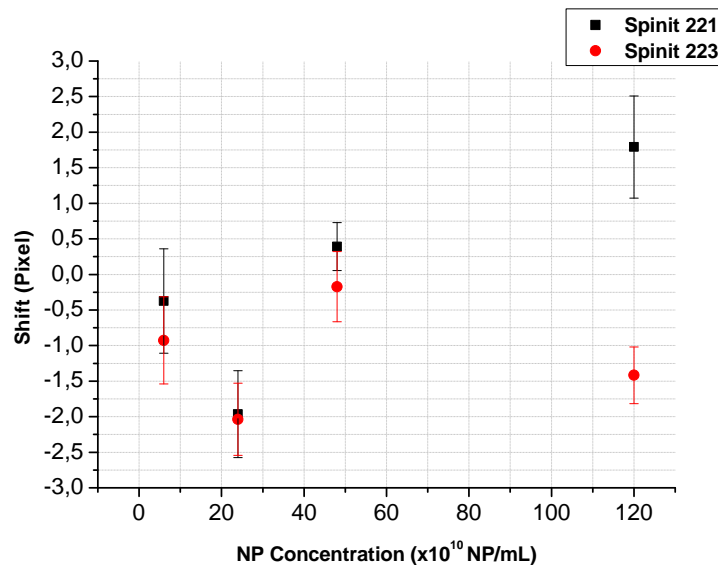


**Figure 3.14:** Nsb for Spinit<sup>®</sup> 221 (with magnet) and Spinit<sup>®</sup> 223 (without magnet). Each assay was repeated twice.

It is clear that the non specific binding is controlled in both Spinit<sup>®</sup> with values from 0 to 2 pixel which is basically the precision of the SPR sensing module. The nsb will be overestimated to be 2 pixel and this value will be considered the noise level of this system. Figure 3.14 confirms the expectation that

there would be an increase in the non specific interaction for higher concentrations reaching 1.8 pixel.

The first test to confirm the effectiveness of the magnet implementation was a 20 minutes assay at 1600 RPM, using a saturated concentration of both streptavidin and bsa-bt to serve as a biological recognition layer (brl). Five different concentrations of nanoparticles were tested: 2.5% , 10%, 20%,50% and 75% of the stock solution ( $2.4 \times 10^{12}$  NP ml<sup>-1</sup>).

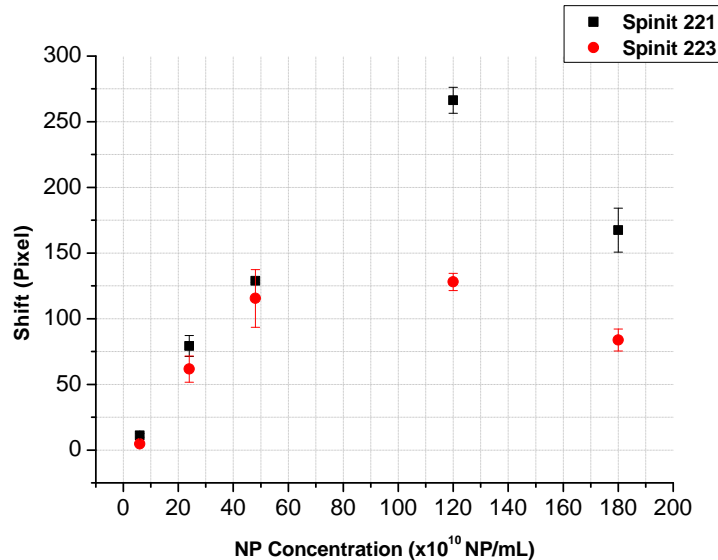


**Figure 3.15:** Comparison between the first zone in each Spinit<sup>®</sup> rotating at 1600 RPM using a saturated biological recognition layer - streptavidin at 100 µg ml<sup>-1</sup> and bsa-bt at 500 µg ml<sup>-1</sup>. Spinit<sup>®</sup> 221 (with magnet) and Spinit<sup>®</sup> 223 (without magnet).

Figure 3.15 shows that the difference between the pixel shift increases as the nanoparticles concentration increases, reaching a maximum near  $1.2 \times 10^{12}$  NP ml<sup>-1</sup> (50% of the stock solution). These results show that increasing the amount of the amplification tags does not lead to an increased association, mainly due to the formation of agglomerates along the microfluidics channels which means a lower number of nanoparticles reaching each sensor and subsequently a lower interaction probability. The increase in terms of shift varies from 11% to 108% reaching its maximum at 50% concentration of the stock solution. Furthermore, the concentration of 50% shows that the system reaches a saturation because the average deviation from each zone is 11 to 18 pixel which represents 4% to 7% of the maximum. In the same way, the overall behaviour is not clearly descendant but on the contrary, it shows an oscillatory behaviour as presented on figure 3.16 which confirms the saturation condition.

An immunoassay is dependent on several variables: the time that it is allowed for the reaction to occur, the binding constants of the elements that are being studied, and the sensor area. Hence, to get a higher number of associations between the recognition element and the target analyte, one may increase the area or work with reactions that are more favourable than others. As the assays is with the interaction between biotin and streptavidin which presents one of the lowest values for the dissociation constant and the sensor surface area is a variable that must be kept constant because it is a requirement for Biosurfit's cartridges, it is possible to increase the interaction time, increasing this way the association probability. To increase the time in which the analyte (bsa-bt) sees the recognition element (streptavidin) and the

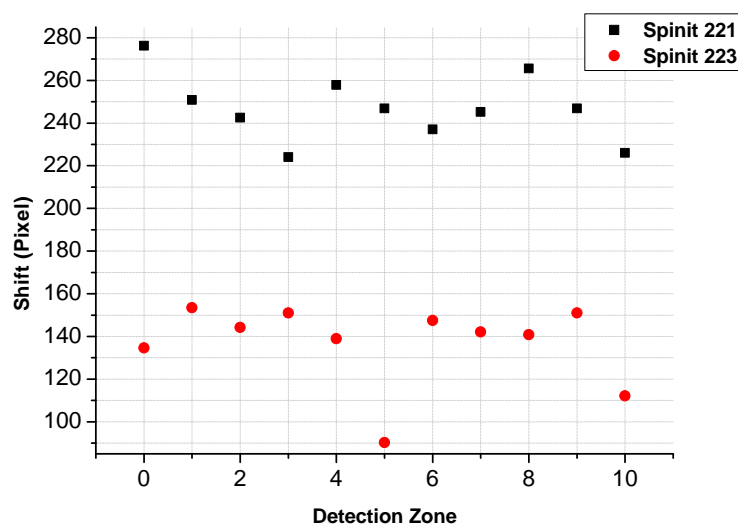


**Figure 3.16:** Shift per detection zone for an assay with streptavidin at  $100 \mu\text{g ml}^{-1}$  and bsa-bt at  $500 \mu\text{g ml}^{-1}$ , and nanoparticles at  $1.2 \times 10^{12} \text{NP ml}^{-1}$ . Spinit<sup>®</sup> 221 (with magnet) and Spinit<sup>®</sup> 223 (without magnet).

time the nanoparticles have to interact with the bsa-bt, the rotating speed can be decreased and provide a higher interaction time. To test this hypothesis, a speed approximately 25% lower was applied to system and the five concentrations tested for the 1600 RPM were tested with 1240 RPM (Fig. 3.17).

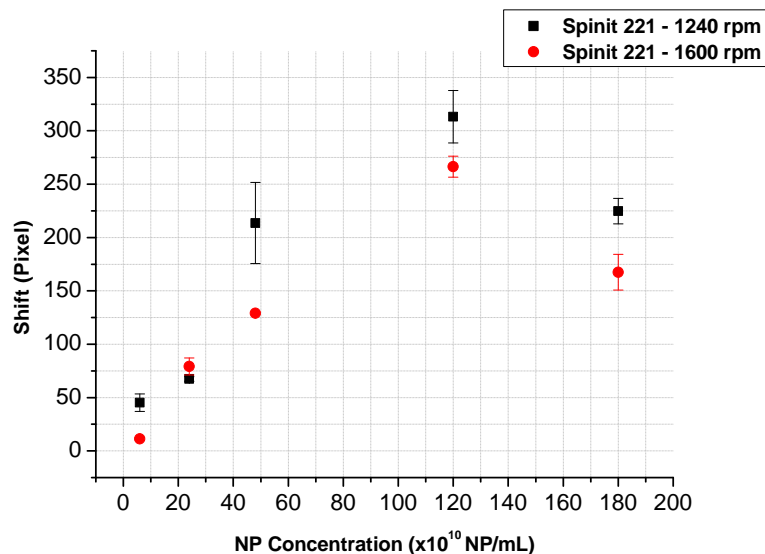


**Figure 3.17:** Comparison of the effect of decreasing the speed of rotation. 1600 RPM are compared to 1240 RPM for the same five concentrations used for figure 3.15. Results regarding zone 0.

Figure 3.17 shows that the overall behaviour is the same for both 1240 RPM and 1600 RPM but with a higher shift, when using a lower speed, as expected. The evidence suggests that using a concentration of  $1.2 \times 10^{12} \text{NP ml}^{-1}$  an optimal point is achieved between the quantity that forms agglomerates and is kept way from the detection zones and the one that actually interacts with the detection zones. Besides, at the concentration  $2.4 \times 10^{10} \text{NP ml}^{-1}$ , there is a clear increase in the shift due to the interaction of

nanoparticles at low speed rather than high speed. At the optimal point, where the shift is higher, there is a 18% increase in terms of shift reducing the speed. Hence, our final assay will be performed rotating at 1240 RPM and during 30 minutes instead of 20 minutes.

It is clear that using nanoparticles with 50% concentration of the stock solution ( $2.4 \times 10^{12}$  NP ml<sup>-1</sup>) the efficiency is maximized. In this assay the recognition element is the streptavidin linked with thiol so it can adhere to the gold surface, the bsa-bt as analyte and the magnetic nanoparticles as amplification tags. This final interaction is possible because each bsa is surrounded, on average, by five biotins so it allows for the connection to both streptavidine from surface and from the nanoparticles.

### 3.4.2 Dynamics Analysis

An assay is limited by the amount of interacting elements on the surface, the time that these elements have to associate, and, ultimately, by the binding capacity - association constant. This constant represents the maximum binding capacity for a certain setup. Magnetic nanoparticles are incorporated into an assay because it allows not only for a higher increase in the effective refractive index but also an increase on the dynamics in case the maximum efficiency is not yet achieved. This number allows to know when a concentration increase is not relevant and therefore an optimal number of nanoparticles to be used is reached, for a specific setup. Furthermore, knowing the binding capacity, there is the possibility to understand how long it takes to a lower binding efficiency to reach the same pixel shift. With this in mind, the maximum of the derivative, which is proportional to the binding capacity is calculated. Additionally, the time until the equilibrium is calculated. The maximum of the derivative is calculated as the centroid, in which the points representing the region of points with the derivative within 95% of  $D_{Max}$  are considered. To calculate the time needed to reach the equilibrium the same method used for the shift calculation was used.

The time needed for the equilibrium was on average 250 seconds which indicates that this time is controlled by the pbs 1X wash after the nanoparticles flow. This time is used to reject some assays that were disturbed by a small flow which led to 400 seconds to reach the equilibrium. The small flow happens when the time that the operator (myself 😊) took to fill the liquids chambers was too high. In addition to the time to reach the equilibrium, the rate at which the association occurred was studied. Figures 3.18, 3.19, 3.20, and 3.21 show the variation of  $D_{Max}$  for all the eleven zones in both Spinit® - with and without magnet.

It is clear that there is a higher binding rate for the first zone and that this rate decreases in the following detection zones. The higher binding rate means that the amount of available nanoparticles, when all sites are free, is higher for the first zones than in the precedent detection zones. This behaviour is characteristic of the disc because it is supposed to occur in a sequential flow of nanoparticles. Figures 3.18, 3.19, 3.20, and 3.21 show that as the bsa-bt concentration increases the rate at which  $D_{Max}$  decreases also increases. This may indicate that for lower concentrations the nanoparticles replacement due to the flow compensates the lost of nanoparticles due to previous binding while for higher concentration the amount that is lost it is higher than the recovered through the flow. To confirm this visual idea that

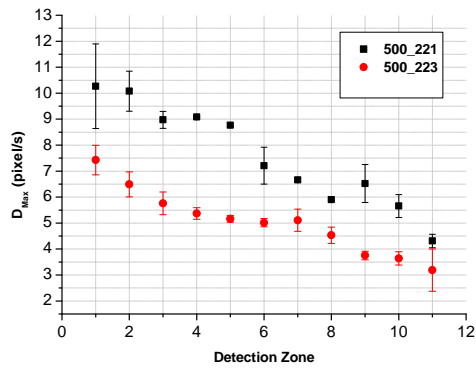


**Figure 3.18:**  $D_{Max}$  for bsa-bt at  $500 \mu\text{g ml}^{-1}$  for Spinit<sup>®</sup> 221 (with magnet) and Spinit<sup>®</sup> 223 (without magnet).

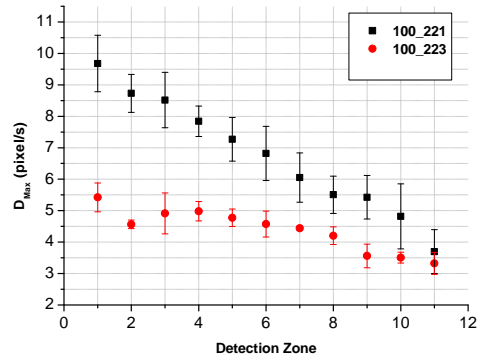


**Figure 3.19:**  $D_{Max}$  for bsa-bt at  $100 \mu\text{g ml}^{-1}$  for Spinit<sup>®</sup> 221 (with magnet) and Spinit<sup>®</sup> 223 (without magnet).

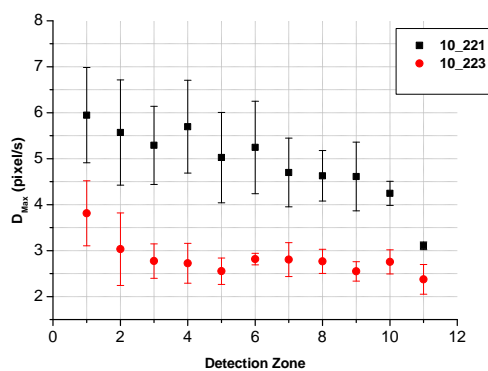


**Figure 3.20:**  $D_{Max}$  for bsa-bt at  $10 \mu\text{g ml}^{-1}$  for Spinit<sup>®</sup> 221 (with magnet) and Spinit<sup>®</sup> 223 (without magnet).

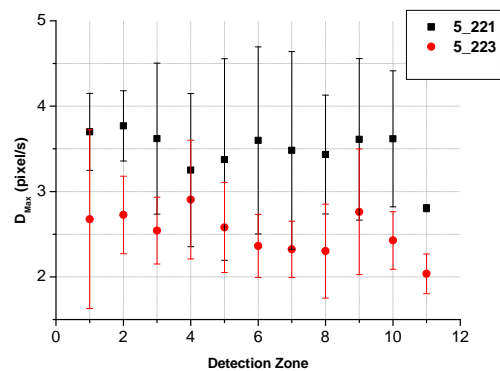


**Figure 3.21:**  $D_{Max}$  for bsa-bt at  $5 \mu\text{g ml}^{-1}$  Spinit<sup>®</sup> 221 (with magnet) and Spinit<sup>®</sup> 223 (without magnet).

the rate at which  $D_{Max}$  decreases is higher for higher concentrations, each curve was fitted to a function described by  $f(x) = ax+b$  and the modulus of the slope ( $|a|$ ) is represented for the different concentrations (Fig. 3.22).

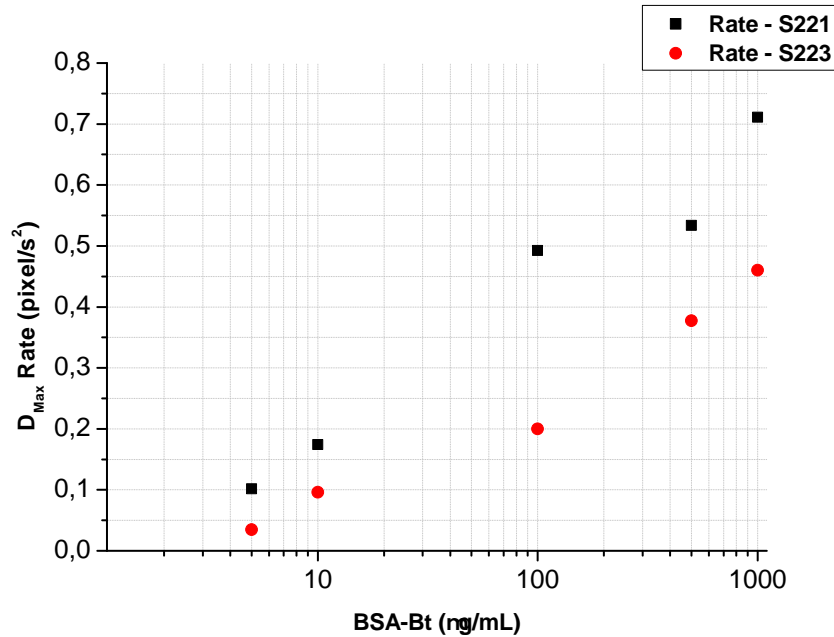


**Figure 3.22:**  $D_{Max}$  variation rate over the 11 detection zones. Spinit<sup>®</sup> 221 (with magnet) and Spinit<sup>®</sup> 223 (without magnet).

Results agree with the visual inspection because higher concentrations lead to a higher slope on the  $D_{Max}$  variation. The shape of the curve is similar in both Spinit<sup>®</sup> but with higher slopes in the Spinit<sup>®</sup> using a magnet. The shape indicates that there is the possibility to further increase the amount of nanoparticles near the surface and expect the rate to not be limited by the physical interaction between the bsa-bt and the nanoparticles.

To calculate the amplification generated by the magnet introduction in terms of the association rate the ratio  $\frac{D_{Max}Spinit221}{D_{Max}Spinit223}$  was calculated. Figure 3.23 shows the representation of this ratio for different zones <sup>1</sup>.

On average the binding rate was increased by a 1.5 factor which means an increase of 50%. On the other hand, the increase does not have a monotonous behaviour, it oscillates without a clear visible pattern so the average can be used as the mean amplification factor.

### 3.4.3 Amplification Analysis

A sensor has a dynamic range associated with it, that is a range of concentrations that it can detect. A sensor exhibits a saturation at both low and high concentrations. At low concentrations, a sensor cannot detect any concentration because there is not a 100% efficiency so there might be none or small analyte interaction which will lead to a imperceptible signal resulting from the nanoparticles and the target analyte. After raising the concentration, the signal starts to increase and will increase more and

<sup>1</sup>The lines connecting the points are only used to improve the visualization. They do not represent any information.

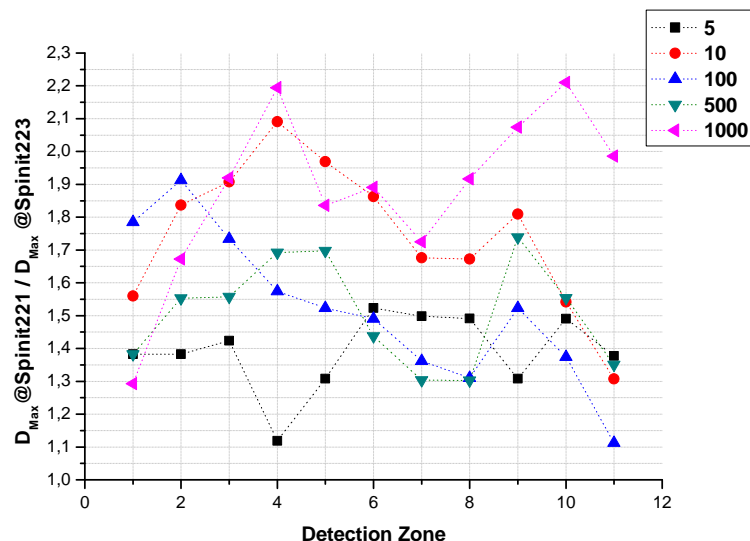


**Figure 3.23:** Association amplification increase with the magnet’s introduction.

more as the amount of analyte increases. Even though this suggests that the more analyte is fed into the system higher would be the shift, that is not possible because of the limited efficiency on the binding capacity. Therefore, there is a concentration at which the system reaches its maximum efficiency and cannot interact with more analyte leading to the signal saturation. In between, there is a S-shaped behaviour from the non detectable plateau to the upper saturation plateau.

Figure 3.24 shows the behaviour for all the eleven zones with respect to bsa-bt’s concentration for the Spinit<sup>®</sup> with magnet. This concentration varies from  $10 \text{ ng ml}^{-1}$  to  $1000 \text{ } \mu\text{g ml}^{-1}$ . Figure 3.25 shows the same assay but performed in the Spinit<sup>®</sup> without magnet. The x axis is showed in a logarithmic scale because the range of values that it covers corresponds to 5 decades which was not perceptible in a linear axis. Each concentration was tested, at least, twice so the average for each zone is taken and the error is estimated as the mean of the difference to mean for each zone.

Despite the fact that this graph is not the best to show how individually each zone is shaped, it is possible to notice that the overall behaviour is similar to a S-shaped curve with a higher detection limit for the magnet implemented Spinit<sup>®</sup>. On the other hand, it seems that it saturates around  $100 \text{ } \mu\text{g ml}^{-1}$ . These two figures allow to see that there is an increase in two aspects: the lower detection limit and the total shift that is obtained. We can see that there is a big error bar associated with the  $10 \text{ } \mu\text{g ml}^{-1}$  and  $100 \text{ } \mu\text{g ml}^{-1}$  due to an assay that has a behaviour different from the other points and increases the error.

To see this behaviour more closely the first and last zone (Fig. 3.26 and Fig. 3.27) are plotted for each Spinit<sup>®</sup>.

Figures 3.26 and 3.27 show that as we go from zone 10 to zone 0 there is not a great difference between the shifts giving the idea that there is not a significant depletion effect. Equally important, the variability associated with the last zone values is much greater than in the rest of the zones, representing 55% for the  $100 \text{ } \mu\text{g ml}^{-1}$  (assay with magnet) and 44% for the  $500 \text{ } \mu\text{g ml}^{-1}$  (assay without magnet), which is mainly associated with a point in which the value was much lower than the rest of the assay and due to the

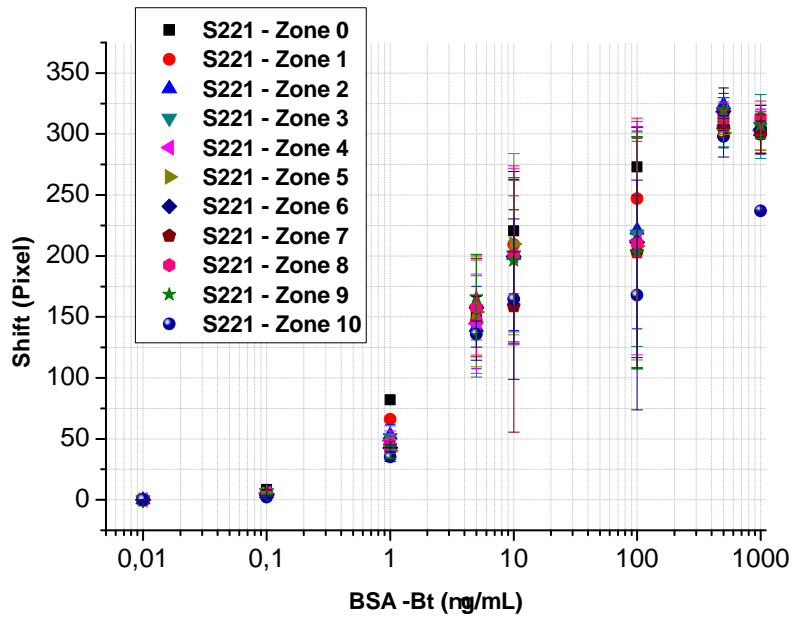


Figure 3.24: Shift per zone for different concentrations of bsa-bt in the Spinit<sup>®</sup> with a magnet.

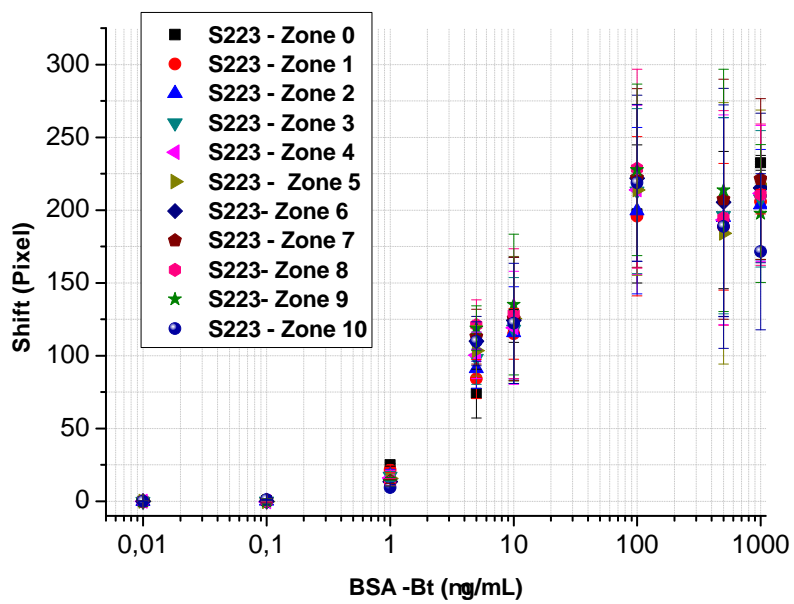
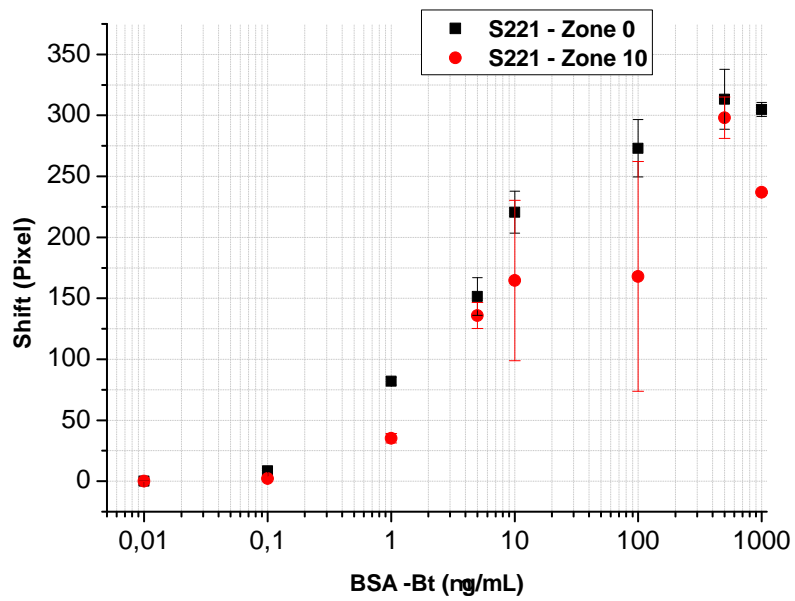
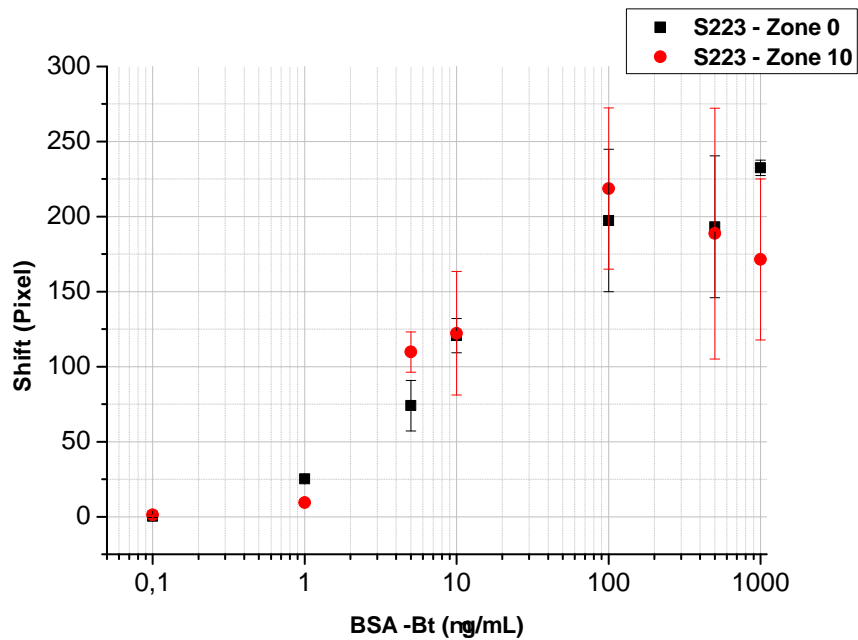


Figure 3.25: Shift per zone for different concentrations of bsa-bt in the Spinit<sup>®</sup> without a magnet.



**Figure 3.26:** Shift in the last and first zone for different concentrations of bsa-bt in the Spinit<sup>®</sup> with a magnet (S221).



**Figure 3.27:** Shift in the last and first zone for different concentrations of bsa-bt in the Spinit<sup>®</sup> without a magnet (S223).

reduced number of assay it has greater impact on the result.

The effect of low depletion needed to be confirmed plotting the relative shift from zones 1 to 10 with respect to zone 0 for both Spinit<sup>®</sup> and each concentration. Figure 3.28 and 3.29 show the relative shift for each zone.

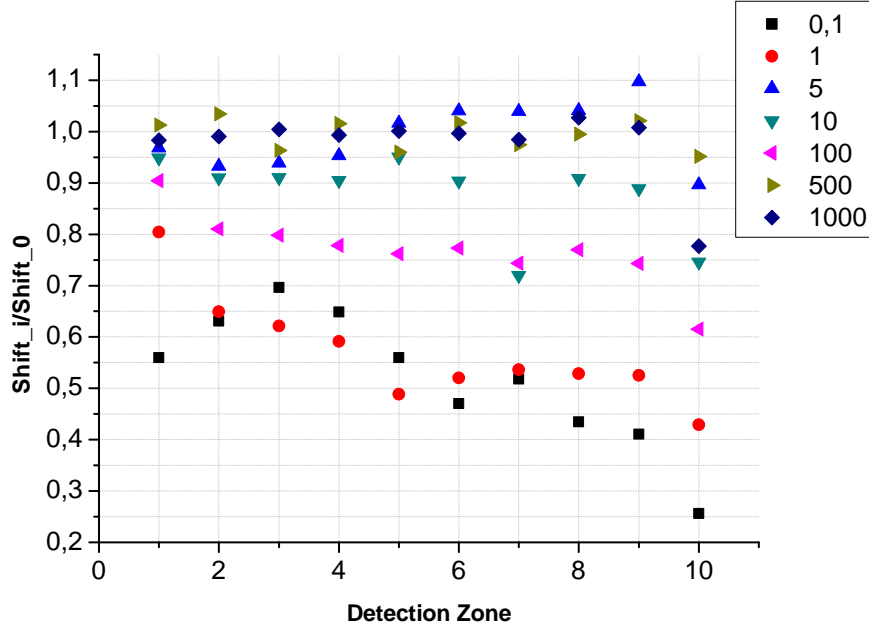


**Figure 3.28:** Relative shift from zone 1 to 10 compared to the first zone for the Spinit<sup>®</sup> with the magnet setup.

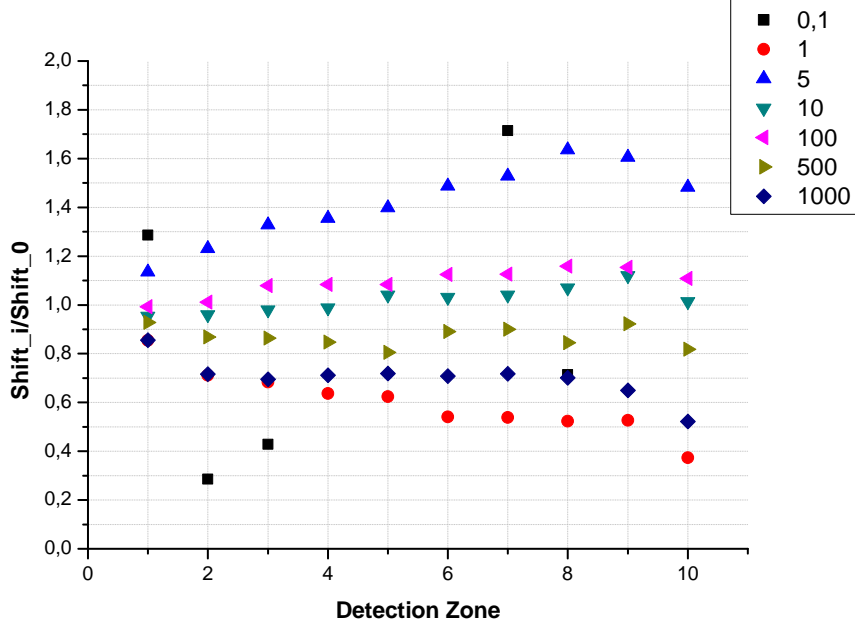
For higher concentrations there is a plateau and the shift is more or less constant for all the 11 detection zones. For the  $1 \mu\text{g ml}^{-1}$  concentration there is an initial depletion until zone 5 than a plateau. Concerning the lowest detectable concentration there is a more clear depletion effect which is mainly due to the reduced amount of bsa-bt available after the interaction in the first zone.

Figure 3.29 shows that there is a plateau and the shift is more or less constant for all the 11 detection zones. The depletion effect is observed for the lower concentrations as it happens for bsa-bt at  $1 \mu\text{g ml}^{-1}$ .

The data that is obtained can be quantified using a fit for each zone. Previously the curve was described as a S-shaped curved which is within the sigmoid functions class. One of the most usual examples is the logistic function given by:

$$y = A_2 + \frac{A_1 - A_2}{1 + \left(\frac{x}{x_0}\right)^p}, \quad x \text{ in } \mu\text{g/mL}, \quad (3.16)$$

where  $y$  represents the pixel shift and  $x$  the concentration of bsa-bt. In this formula  $A_2$  represents the upper saturation asymptote, that is the maximum response that can be expected from the concentration profile. As the concentration decreases the shift decreases following a S-shape. There is a detection limit where the shift response is zero or below the noise level of the configuration which corresponds to  $A_1$ . The  $p$  parameter refers to the Hill's slope which controls the steepness of the curve. In this assay this parameter can only be positive so there is a growth from  $A_1$  to  $A_2$ . Finally,  $x_0$  represents the inflection point that is the maximum of  $y$  derivative with respect to  $x$ . Using other words, is the point the curve



**Figure 3.29:** Relative shift from zone 1 to 10 compared to the first zone for the Spinit<sup>®</sup> without the magnet setup.

changes from being concave upwards to concave downwards. After this point the derivative decreases until  $y=A_2$ , where it is approximately zero.

The expression 3.16 is fitted to every detection zone using the experimental data with and without magnet. The results are presented in appendix. Figure 3.30 shows the fits for zone 0 using both configurations.

First, the comparison between zone 0 from each setup are shown because these zones are in the same conditions for both assays and, one more time, it was not worthwhile to show every single zone. Figure 3.30 shows that the theoretical curve fits well into the experimental data ( $R^2 = 0.99$ ). In addition, the pixel shift is higher when using the magnet rather than when it is not used. The increase is minimum for the higher concentration with an increase of 31.7% and is maximum for the lower concentration with a shift of more than 2300 %. Both experimental data and theoretical fit suggest that, considering the error bars, the assay reaches its saturation at  $100 \mu\text{g ml}^{-1}$  of bsa-bt. To further check the detection limit and show that there is a significant difference between not having a magnet and the new setup improvement, a zoom of the region near the  $100 \text{ ng ml}^{-1}$  is presented in figure 3.31.

The green line represents the noise level that is calculated based on the maximum of the nsb. We can see that the value obtained with the new setup, besides being higher than the one obtained using the previous setup, it is four times higher than the noise level which corresponds to a 40 sigma deviation from the average.

Finally, using the results from the fits we can use the saturation concentration for both configurations and calculate the amplification based on that value. The amplification is defined as

$$\frac{Shift_{with\ magnet}}{Shift_{without\ magnet}}. \quad (3.17)$$

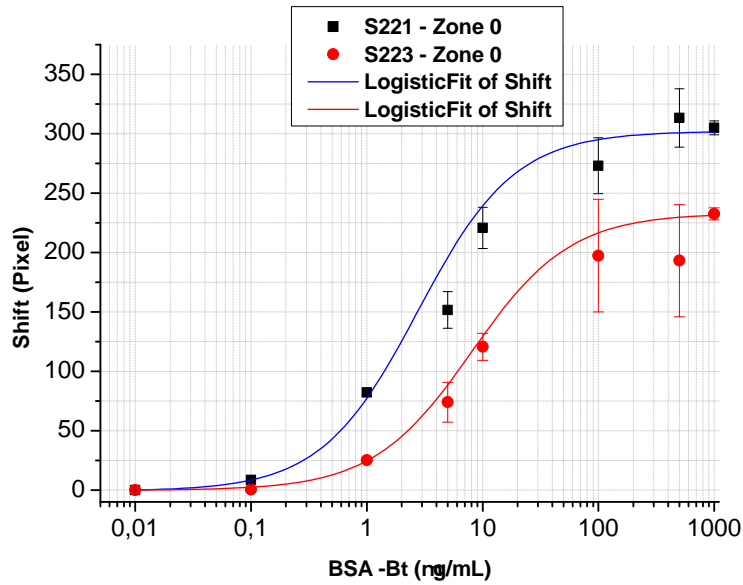


**Figure 3.30:** Logistic fit to zone 0 for both setups: with and without a magnet. Disk rotating approximately 1240 RPM. Spinit<sup>®</sup> 221 (with magnet) and Spinit<sup>®</sup> 223 (without magnet).

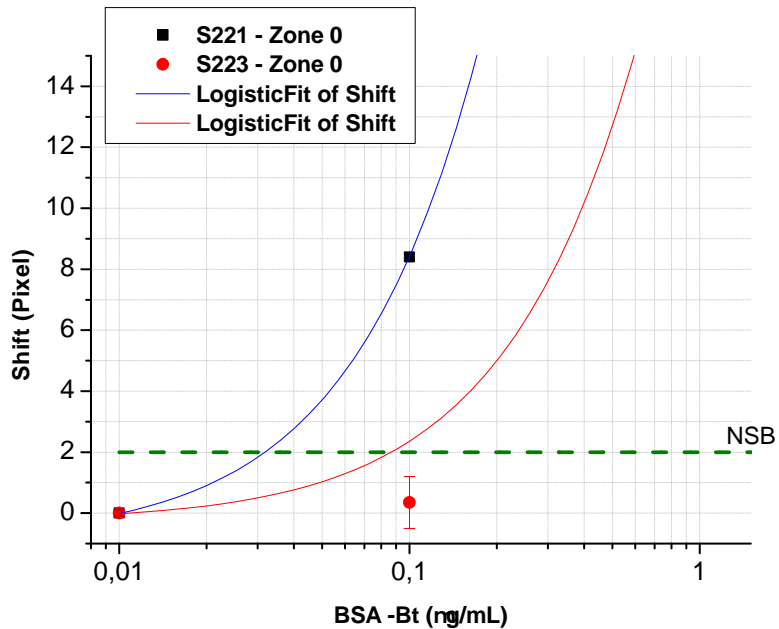


**Figure 3.31:** Logistic fit to zone 0 for both setups. Zoom into the detection limit zone. Spinit<sup>®</sup> 221 (with magnet) and Spinit<sup>®</sup> 223 (without magnet).

To apply this formula, the parameter  $A_2$  that resulted from the fits was used for the 5 point. This value is calculated for each zone and for both setups. Figure 3.32 represents the expression 3.17 for five different concentrations.

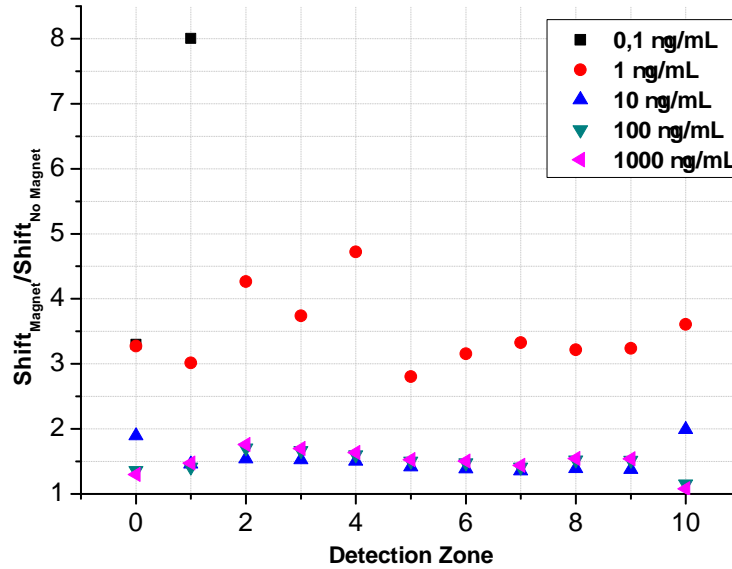


Figure 3.32: Amplification calculation using the fitted results.

It is important to notice that for the lowest concentration only two points are presented. This can be explained, not by the great amplification but due to the values obtained for the shift without magnet being close to zero so the amplification value increases immensely. The amplification for the lower concentration is approximately 3.3 for zone 0. When using  $1 \mu\text{g ml}^{-1}$ , we can observe that the signal amplification fluctuates with an average amplification of 3.48. For the higher concentrations the oscillations are less notorious. It continues to fluctuate for  $10 \mu\text{g ml}^{-1}$ ,  $100 \mu\text{g ml}^{-1}$ , and  $1000 \mu\text{g ml}^{-1}$  but now with an average value that represents an increase of 50% relative to the non magnet configuration.

# Conclusions

---

Biosensors are devices that detect several biological elements. One of the most important applications concerns the clinical diagnostics. There is a demand for faster diagnostics which will help to give a more effective treatment to the patient. Therefore biosensors face the challenge of reducing the time to detect biological elements and at the same time to give accurate results for all conventional blood tests. Our objective with this thesis is to develop a magnetic nanoparticle assay and demonstrate its feasibility using a nouvelle magnetic manipulation system and using a new diffraction grating.

First, we simulate a grating optimized for a setup that uses a SPR angle within  $10^\circ$  so it is possible to apply a method of analysis that uses not only the angular shift but also area variations because near  $0^\circ$  the area variations are greater. In addition, this allows for the utilization of a dvd-pickup which already uses a 650 nm laser and is a robust and well tested system. We simulate the grating using a fixed wavelength of 650 nm and calculate its sensitivity for both bulk changes and surface changes. Using this approach the overall sensitivity in terms of angular shift, defined as the surface sensitivity divided by the bulk sensitivity, shows values from 0.4 to 0.54 for the selected gratings. This is not the best metric because the signal quality in terms of contrast and FWHM is neglected. The factor associated with these two elements is included showing that there is a higher sensitivity for the grating with a period of 800 nm, right and left frequency equal to 3.25 and ridge of 115 nm. This grating was produced by Synchronicity Mastering Services twice due to the mother and son stamper different definitions. The final result is within the 10% error margin which we considered acceptable. These gratings were not tested because they arrived in the end of June and the full analysis was only available in the middle of July. As the magnetic system was already incorporated within Spinit<sup>®</sup>, the new setup was not developed and only the magnetic implementation is tested.

We tested the magnetic nanoparticles implementation with a setup that uses the same SPR module used by the Spinit<sup>®</sup> but without the rotating system so the system is fed with a peristaltic pump and the detection zone position is tuned by hand. This setup allows for the selection of the magnet and the magnetic nanoparticles supplier. Further investigations on the assay shows that the assay yields a high non specific binding therefore leading to a higher imprecision in the final results.

We see that the liquids sequencing disk allows to increase the rapidity and easiness of the testing of new assay configurations. We tested two different assays to implement magnetic nanoparticles. Both assays were based on the high association constant between biotin and streptavidin. We observe that the assay is more controlled when we use streptavidin with thiol to functionalize the surface rather than the unspecific interaction of bsa-bt with the gold sensor.

We designed and built a prototype that can handle three magnets allocated at the same radius and protected with a non reflective adhesive tape so there is not reflected light coming from the upper part of the magnet. This design is implemented into Spinit<sup>®</sup>, without any structural change besides the position of the pickup, which means that the usual tests are not compromised by this infrastructure.

We aim to maximize the pixel shift due to the magnetic nanoparticle amplification therefore we test different concentrations of nanoparticles using both Spinit<sup>®</sup> (with and without a magnet) at 1600 RPM. Results show that there is parabolic shape for the shift and the maximum in shift is observed when using  $1.2 \times 10^{12}$  NP ml<sup>-1</sup> with a shift two times larger than the one observed without using the magnet. There was an effect of agglomeration causing high losses along the microfluidic channels that was higher for the higher concentrations which explain this parabolic shape.

An immunoassay depends on the probability of interaction which is increased by the time in which two elements have to react. We test this time by decreasing the speed of rotation from 1600 RPM to 1240 RPM. The assays are repeated using a saturated biological recognition layer, leading to an increase of 18% compared with a rotation at 1600 RPM.

This assay has some peculiarities because it does not present the usual depletion effect that we would expect from a successive interaction such as the present one. We would expect that the second zone would have a lower shift because part of the nanoparticles interacted in the first zone. This can be explained by the size of the nanoparticles (hydrodynamic diameter = 120 nm) which leads to a larger area coverage per nanoparticle hindering the association of other nanoparticles that are left in enough number to saturate equally the following detection zones.

Furthermore, we calculate the time for the magnetic nanoparticle interaction to stabilize and the results show that there is not a clear difference between using or not using a magnetic for the time needed to reach the saturation. The dynamics analysis show that the association is not limited by the binding capacity of the nanoparticles to the bsa-bt on the surface because for the saturating conditions  $D_{Max}$  increases as the amount of nanoparticles increase. This means that the amount of nanoparticles can be further increased leading to a higher association rate, which may reduce the time needed to perform the assay. The prove that the amount of nanoparticle decreases is that the rate at which the  $D_{Max}$  decreases is higher for the higher concentrations which means that for these concentrations, more nanoparticles are binding leading to less nanoparticles available for the following zones. This behaviour suggests that the resuspension due to the flow is enough to compensate the nanoparticles lost for the lower concentrations but not for the larger concentrations.

We test several concentrations of bsa-bt: from 10 ng ml<sup>-1</sup> up to 1000 µg ml<sup>-1</sup>. The experimental data shows that the LOD is improved from approximately 1 µg ml<sup>-1</sup> to 100 ng ml<sup>-1</sup> which means a 10 fold improvement in the detection limit with the magnetic actuation system for an immunoassay using 120 nm diameter nanoparticles coated with streptavidin as an amplification tag and bsa-bt as analyte.

The points from each zone were fitted with a logistic function and the parameters from the fit are used to calculate the shift amplification. A 50% increase in shift is obtained, when using a magnet, for the higher concentrations, and a 200% increase when using lower concentrations (100 ng ml<sup>-1</sup> and 1 µg ml<sup>-1</sup>).

Combining the results from the dynamics analysis and the amplification analysis, we can understand

that despite the fact the association rate is higher in the first zones, the shift is the same for all the zones which is explained by the duration of the assay. Passing the nanoparticles during 250 seconds there is time to saturate the binding sites.

In this work the magnetic nanoparticle implementation is achieved with success showing a 10 fold increase in the detection limit using a versatile and adaptable prototype which allows the usage of magnets with different diameters and shapes.

## 4.1 Future Work

One of the goals of this project was to build a new setup which would use a different detection module. This module would use an incidence angle within  $10^\circ$  but it was not possible to build it due to delays on the grating manufacturing. The gratings are ready and approved therefore this setup should be implemented applying new algorithms to increase the sensitivity.

Studies to show the effect of the magnetic field in the electronics should be carried on to see if there are major concerns and to check if any magnetic shielding is necessary. The magnets being used were the strongest ones considering the standard magnets available so a customized magnet with higher magnetic forces should be tested.

There is still some variability associated with the measurements that can be mitigated using a protocol before using the magnetic nanoparticles that avoids the formation of agglomerates. In addition there are some slow flow problems that need to be addressed.

Furthermore, when comparing the results with the current detection capabilities ( $37.5 \text{ ng ml}^{-1}$  for the C-Reactive protein), the result is far from being better, however it is important to notice that there is no optimization in terms of buffer's pH so this analysis is also suggested. There is also the competition with the surfynol which hinders the streptavidin+thiol binding to the surface so new discs, which do not need surfynol and are now available should be used.



# Bibliography

---

- [1] R. Bashir. BioMEMS: state-of-the-art in detection, opportunities and prospects. *Advanced drug delivery reviews*, 56(11):1565–86, 2004. ISSN 0169-409X. doi: 10.1016/j.addr.2004.03.002.
- [2] Biosurfit. spinit reader and spinit cartridges technical information, 2013.
- [3] D. Bohm and D. Pines. A collective description of electron interactions. i. magnetic interactions. *Phys. Rev.*, 82(5):625–634, June 1951. doi: 10.1103/PhysRev.82.625. URL <http://link.aps.org/doi/10.1103/PhysRev.82.625>.
- [4] S. BT SHAHIR. Biosensor technology, 2010.
- [5] J. P. Chambers, B. P. Arulanandam, L. L. Matta, A. Weis, and J. J. Valdes. Biosensor recognition elements. *Curr Issues Mol Biol*, 10(1-2):1–12, 2008. ISSN 1467-3037.
- [6] S. D. Choudhury, R. Badugu, K. Ray, P. S. Vanam, and J. R. Lakowicz. Fluorescence enhancement using silver-gold nanocomposite substrates. *Proc SPIE*, 8234:82340B, Feb. 2012. ISSN 1996-756X. doi: 10.1117/12.924603. URL <http://www.ncbi.nlm.nih.gov/pmc/articles/PMC3766972/>.
- [7] L. C. Clark and C. Lyons. Electrode systems for continuous monitoring in cardiovascular surgery. *Ann. N. Y. Acad. Sci.*, 102:29–45, Oct. 1962. ISSN 0077-8923.
- [8] U. FANO. The theory of anomalous diffraction gratings and of quasi-stationary waves on metallic surfaces (sommerfeld s waves). *J. Opt. Soc. Am.*, 31(3):213–222, Mar. 1941. doi: 10.1364/JOSA.31.000213. URL <http://www.opticsinfobase.org/abstract.cfm?URI=josa-31-3-213>.
- [9] E. Fu, T. Chinowsky, K. Nelson, and P. Yager. Chapter 10. SPR imaging for clinical diagnostics. In R. B. M. Schasfoort and A. J. Tudos, editors, *Handbook of Surface Plasmon Resonance*, pages 313–332. Royal Society of Chemistry, Cambridge, 2008. ISBN 978-0-85404-267-8. URL <http://ebook.rsc.org/?DOI=10.1039/9781847558220-00313>.
- [10] M. A. M. Gijs. Magnetic bead handling on-chip: new opportunities for analytical applications. *Microfluidics and Nanofluidics*, Oct. 2004. ISSN 1613-4982, 1613-4990. doi: 10.1007/s10404-004-0010-y. URL <http://infoscience.epfl.ch/record/55909>.
- [11] A. N. Grigorenko, M. Polini, and K. S. Novoselov. Graphene plasmonics. *Nat Photon*, 6(11):749–758, Nov. 2012. ISSN 1749-4885. doi: 10.1038/nphoton.2012.262. URL <http://www.nature.com/nphoton/journal/v6/n11/abs/nphoton.2012.262.html>.

- [12] J. Homola. Electromagnetic theory of surface plasmons. In J. Homola, editor, *Surface Plasmon Resonance Based Sensors*, number 4 in Springer Series on Chemical Sensors and Biosensors, pages 3–44. Springer Berlin Heidelberg, Jan. 2006. ISBN 978-3-540-33918-2, 978-3-540-33919-9. URL [http://link.springer.com/chapter/10.1007/5346\\_013](http://link.springer.com/chapter/10.1007/5346_013).
- [13] M.-G. Kim, Y.-B. Shin, J.-M. Jung, H.-S. Ro, and B. H. Chung. Enhanced sensitivity of surface plasmon resonance (SPR) immunoassays using a peroxidase-catalyzed precipitation reaction and its application to a protein microarray. *J. Immunol. Methods*, 297(1-2):125–132, Feb. 2005. ISSN 0022-1759. doi: 10.1016/j.jim.2004.12.007.
- [14] V. G. Kravets, F. Schedin, R. Jalil, L. Britnell, R. V. Gorbachev, D. Ansell, B. Thackray, K. S. Novoselov, A. K. Geim, A. V. Kabashin, and A. N. Grigorenko. Singular phase nano-optics in plasmonic metamaterials for label-free single-molecule detection. *Nat Mater*, 12(4):304–309, Apr. 2013. ISSN 1476-1122. doi: 10.1038/nmat3537. URL <http://www.nature.com/nmat/journal/v12/n4/full/nmat3537.html>.
- [15] E. Kretschmann and H. Raether. Radiative decay of nonradiative surface plasmons excited by light. *Z. Naturforsch. A*, 23:2135, 1968.
- [16] W.-C. Law, K.-T. Yong, A. Baev, R. Hu, and P. N. Prasad. Nanoparticle enhanced surface plasmon resonance biosensing: Application of gold nanorods. *Optics Express*, 17(21):19041, Oct. 2009. ISSN 1094-4087. doi: 10.1364/OE.17.019041. URL <http://www.opticsinfobase.org/oe/fulltext.cfm?uri=oe-17-21-19041&id=186505>.
- [17] E. G. Lee, K. M. Park, J. Y. Jeong, S. H. Lee, J. E. Baek, H. W. Lee, J. K. Jung, and B. H. Chung. Carbon nanotube-assisted enhancement of surface plasmon resonance signal. *Analytical Biochemistry*, 408(2):206–211, Jan. 2011. ISSN 0003-2697. doi: 10.1016/j.ab.2010.09.026. URL <http://www.sciencedirect.com/science/article/pii/S0003269710006111>.
- [18] P. B. Lippa, C. M. Ållner, A. Schlichtiger, and H. Schlebusch. Point-of-care testing (POCT): Current techniques and future perspectives. *TrAC Trends in Analytical Chemistry*, 30(6):887–898, June 2011. ISSN 0165-9936. doi: 10.1016/j.trac.2011.01.019. URL <http://www.sciencedirect.com/science/article/pii/S0165993611000860>.
- [19] L. A. Lyon, M. D. Musick, and M. J. Natan. Colloidal au-enhanced surface plasmon resonance immunosensing. *Anal. Chem.*, 70(24):5177–5183, Dec. 1998. ISSN 0003-2700. doi: 10.1021/ac9809940. URL <http://dx.doi.org/10.1021/ac9809940>.
- [20] S. A. Maier. *Plasmonics: Fundamentals and Applications: Fundamentals and Applications*. Springer Science & Business Media, May 2007. ISBN 9780387378251.
- [21] Y. Moser. *Dynamic Actuation of Magnetic Beads for Immunoassays on-chip*. PhD thesis, Lausanne, 2010.

- [22] A. H. Nicol. Grating coupled surface plasmon enhanced fluorescence spectroscopy, 2006. URL <http://ubm.opus.hbz-nrw.de/volltexte/2006/932/>.
- [23] A. Otto. Excitation of nonradiative surface plasma waves in silver by the method of frustrated total reflection. *Z. Physik*, 216(4):398–410, Aug. 1968. ISSN 0044-3328. doi: 10.1007/BF01391532. URL <http://link.springer.com/article/10.1007/BF01391532>.
- [24] S. A. Peyman, A. Iles, and N. Pamme. Mobile magnetic particles as solid-supports for rapid surface-based bioanalysis in continuous flow. *Lab Chip*, 9(21):3110–3117, Nov. 2009. ISSN 1473-0189. doi: 10.1039/B904724G. URL <http://pubs.rsc.org/en/content/articlelanding/2009/lc/b904724g>.
- [25] M. Riskin, R. Tel-Vered, O. Lioubashevski, and I. Willner. Ultrasensitive surface plasmon resonance detection of trinitrotoluene by a bis-aniline-cross-linked au nanoparticles composite. *J. Am. Chem. Soc.*, 131(21):7368–7378, June 2009. ISSN 0002-7863. doi: 10.1021/ja9001212. URL <http://dx.doi.org/10.1021/ja9001212>.
- [26] R. H. Ritchie. Plasma losses by fast electrons in thin films. *Physical Review*, 106:874–881, June 1957. ISSN 1536-6065. doi: 10.1103/PhysRev.106.874. URL <http://adsabs.harvard.edu/abs/1957PhRv..106..874R>.
- [27] O. Salihoglu, S. Balci, and C. Kocabas. Plasmon-polaritons on graphene-metal surface and their use in biosensors. *Applied Physics Letters*, 100(21):213110, May 2012. ISSN 0003-6951, 1077-3118. doi: 10.1063/1.4721453. URL <http://scitation.aip.org/content/aip/journal/apl/100/21/10.1063/1.4721453>.
- [28] S. Sang, W. Zhang, and Y. Zhao. Review on the design art of biosensors. In T. Rinken, editor, *State of the Art in Biosensors - General Aspects*. InTech, Mar. 2013. ISBN 978-953-51-1004-0. URL <http://www.intechopen.com/books/state-of-the-art-in-biosensors-general-aspects/review-on-the-design-art-of-biosensors>.
- [29] S. D. Soelberg and C. E. Furlong. Biosensors and bioassays for ecological risk monitoring and assessment. In E. A. Laws, editor, *Environmental Toxicology*, pages 121–142. Springer New York, Jan. 2013. ISBN 978-1-4614-5763-3, 978-1-4614-5764-0. URL [http://link.springer.com/chapter/10.1007/978-1-4614-5764-0\\_6](http://link.springer.com/chapter/10.1007/978-1-4614-5764-0_6).
- [30] Y. Teramura, Y. Arima, and H. Iwata. Surface plasmon resonance-based highly sensitive immunosensing for brain natriuretic peptide using nanobeads for signal amplification. *Analytical Biochemistry*, 357(2):208–215, Oct. 2006. ISSN 0003-2697. doi: 10.1016/j.ab.2006.07.032. URL <http://www.sciencedirect.com/science/article/pii/S0003269706005409>.
- [31] M. Thompson, L.-E. Cheran, and S. Sadeghi. *Sensor Technology in Neuroscience*. Royal Society of Chemistry, 2013. ISBN 9781849733793.
- [32] A. P. F. Turner. Biosensors: sense and sensibility. *Chem. Soc. Rev.*, 42(8):3184–3196, Mar. 2013. ISSN 1460-4744. doi: 10.1039/C3CS35528D. URL <http://pubs.rsc.org/en/content/articlelanding/2013/cs/c3cs35528d>.

- [33] P. von Lode. Point-of-care immunotesting: Approaching the analytical performance of central laboratory methods. *Clinical Biochemistry*, 38(7):591–606, July 2005. ISSN 0009-9120. doi: 10.1016/j.clinbiochem.2005.03.008. URL <http://www.sciencedirect.com/science/article/pii/S0009912005000895>.
- [34] J. Wang, A. Munir, Z. Zhu, and H. S. Zhou. Magnetic nanoparticle enhanced surface plasmon resonance sensing and its application for the ultrasensitive detection of magnetic nanoparticle-enriched small molecules. *Anal. Chem.*, 82(16):6782–6789, Aug. 2010. ISSN 0003-2700. doi: 10.1021/ac100812c. URL <http://dx.doi.org/10.1021/ac100812c>.
- [35] Y. Wang, J. Dostalek, and W. Knoll. Magnetic nanoparticle-enhanced biosensor based on grating-coupled surface plasmon resonance. *Anal. Chem.*, 83(16):6202–6207, Aug. 2011. ISSN 0003-2700. doi: 10.1021/ac200751s. URL <http://dx.doi.org/10.1021/ac200751s>.
- [36] R. W. Wood. On a remarkable case of uneven distribution of light in a diffraction grating spectrum. *Proc. Phys. Soc. London*, 18(1):269, June 1902. ISSN 1478-7814. doi: 10.1088/1478-7814/18/1/325. URL <http://iopscience.iop.org/1478-7814/18/1/325>.
- [37] S. Zeng, X. Yu, W.-C. Law, Y. Zhang, R. Hu, X.-Q. Dinh, H.-P. Ho, and K.-T. Yong. Size dependence of au NP-enhanced surface plasmon resonance based on differential phase measurement. *Sensors and Actuators B: Chemical*, 176:1128–1133, Jan. 2013. ISSN 0925-4005. doi: 10.1016/j.snb.2012.09.073. URL <http://www.sciencedirect.com/science/article/pii/S0925400512009860>.
- [38] S. Zeng, D. Baillargeat, H.-P. Ho, and K.-T. Yong. Nanomaterials enhanced surface plasmon resonance for biological and chemical sensing applications. *Chem. Soc. Rev.*, 43(10):3426–3452, Apr. 2014. ISSN 1460-4744. doi: 10.1039/C3CS60479A. URL <http://pubs.rsc.org/en/content/articlelanding/2014/cs/c3cs60479a>.